LUT UNIVERSITY
LUT School of Energy Systems
LUT Mechanical Engineering

Janne Martikainen

REAL-TIME SIMULATION OF CONTINUOUS FLIGHT AUGERING AND FULL DISPLACEMENT PILING IN MULTILAYERED SOIL

Examiners: Professor Aki Mikkola
D. Sc. (Tech.) Kimmo Kerkkänen

TIIVISTELMÄ

LUT-Yliopisto
LUT School of Energy Systems
LUT Kone

Janne Martikainen

Jatkuvakierteisen kairauksen ja syrjäyttävän porapaalutuksen reaaliaikasimulointi monikerroksisessa maaperässä

Diplomityö

2021

67 sivua, 35 kuvaa, 4 taulukkoa ja 3 liitettä

Tarkastajat: Professori Aki Mikkola
TkT Kimmo Kerkkänen

Hakusanat: CFA, FDP, poraus, reaaliaikasimulointi, monikappaledynamiikka, yhteissimulointi

Tämän työn tavoitteena on kehittää parametrisoitu reaaliaikainen simulaatiomalli MPx90-monikäyttökoneelle jatkuvakierteisen kairauksen ja syrjäyttävän porapaalutuksen työmenetelmille monikerroksisessa maaperässä. Työ tehtiin Junttan Oy:lle.

Aluksi etsitään olemassa olevaa tutkimustietoa porausprosessien aikaisesta kuormituksesta kirjallisuuskatsauksen avulla. Tulosten perusteella kehitetään analyyttiset mallit porauksen aikaisen voiman ja väännön laskemiseksi. Mevea-ohjelmistolla mallinnetaan koneesta yksinkertaistettu malli, joka sisältää vain porauksessa tarvittavat ominaisuudet. Koska Mevealla ei voida mallintaa porausta monikerroksisessa maaperässä, porausprosessi mallinnetaan yhteissimuloinnilla. Mahdollisiksi ohjelmistoiksi tähän valittiin Xcos ja Simulink, joiden suorituskykyä vertaamalla yhteissimulointiohjelmistoksi valittiin lopulta Simulink. Simulaatiomallit validoidaan vertaamalla simulaatiotuloksia koeporausten mittausdataan.

Simulaatiotulosten vertailu mittausdataan osoitti mallien laskevan porauskuormituksen riittävällä tarkkuudella. Molemmat mallit laskivat väännön hyvällä tarkkuudella, mutta voiman osalta tarkkuus oli heikompi. Molemmat mallit toimivat reaaliajassa ja työn tavoitteet saavutettiin.

Tulevaisuudessa tarvitaan jatkotutkimusta prosessimallien tarkkuuden parantamiseksi ja uusien mallien kehittämiseksi muille työmenetelmille. Kehitettyä Mevea-mallia voidaan jatkossa käyttää perustana koko MPx90-koneen reaaliaikamallin kehitykselle.

ABSTRACT

LUT University
LUT School of Energy Systems
LUT Mechanical Engineering

Janne Martikainen

Real-time simulation of continuous flight augering and full displacement piling in multilayered soil

Master's thesis

2021

67 pages, 35 figures, 4 tables and 3 appendices

Examiners: Professor Aki Mikkola
D. Sc. (Tech.) Kimmo Kerkkänen

Keywords: CFA, FDP, drilling, real-time simulation, multibody dynamics, co-simulation

The goal of this thesis is to develop a parametrized real-time simulation model of continuous flight augering and full displacement piling in multilayered soil for an MPx90 multipurpose drilling rig. This thesis was made for Junttan Oy.

A literature review is first conducted to gain an understanding about the causes of drilling loads during the processes. These results are then used to develop analytical models for calculating force and torque during drilling. A simplified model of the machine, which only the features required for drilling, is modelled with Mevea software. As drilling in soils with multiple layers cannot be modelled with Mevea, the drilling process is modelled utilizing co-simulation. The co-simulation software for the process models is selected to be Simulink from performance comparisons between Xcos and Simulink. Validation of the simulation models is done by comparing simulation results with measurement data obtained from test drilling.

Comparing the simulation results with measurement data showed that the models calculate the drilling loads with sufficient accuracy. Simulated torque with both models had good accuracy while the simulated force was more lacking in accuracy. Both models run in real-time and the goals of the thesis were reached.

In the future, more research is needed to improve the accuracy of the process models and develop models for other drilling methods. The developed Mevea model can be used as a basis for developing a full real-time model of the MPx90 machine.

ACKNOWLEDGEMENTS

This thesis was made for Junttan Oy during 2020–2021. I would like to thank everyone at Junttan who was involved in making this thesis for their guidance and support, and for giving me this opportunity. I also thank the examiners of this thesis, Professor Aki Mikkola and Dr. Kimmo Kerkkänen.

Janne Martikainen
Kuopio, 27.5.2021

TABLE OF CONTENTS

LIST OF SYMBOLS AND ABBREVIATIONS

a	Acceleration of soil being cut [m/s^2]
a_c	Net area ratio
a_r	Reduction factor
B_q	Pore pressure ratio
c	Cohesion of soil [Pa]
c'	Effective cohesion of soil [Pa]
c_a	Adhesion between soil and drill bit [Pa]
D_{s0}	Auger shaft minimum diameter [m]
D_s	Displacement part diameter [m]
d	Cut per revolution [m/r]
d_c	Critical depth [m]
F	Penetration force [N]
F_a	Penetration force of auger [N]
F_b	Penetration force of drill bit [N]
F_r	Centrifugal force [N]
f_1	Friction force on surface 1 [N]
f_2	Friction force on surface 2 [N]
f_3	Friction force on surface 3 [N]
f_4	Friction force on surface 4 [N]
f_s	Sleeve friction [Pa]
G	Soil element weight [N]
g	Gravitational acceleration [m/s^2]
H_2	Force component in the horizontal cutting direction [N]
H_b	Horizontal cutter force [N]
h_s	Auger length [m]
$h_{s;i}$	Auger section length [m]
K_0	Coefficient of active earth pressure
l	Auger flute width [m]
M_T	Total FDP torque [Nm]
M_{Tb}	Torque in the FDP auger tip [Nm]

M_{Ts}	Torque in the FDP auger shaft [Nm]
m_{Ts}	Torque coefficient
N	Number of auger helices
N_1	Normal pressure force on surface 1 [N]
N_2	Normal pressure force on surface 2 [N]
N_{a1}	Constant
N_{c1}	Constant
N_{ca1}	Constant
N_{q1}	Constant
$N_{\rho 1}$	Constant
N_{c2}	Constant
N_{q2}	Constant
$N_{\rho 2}$	Constant
N_{c3}	Constant
N_{q3}	Constant
$N_{\rho 3}$	Constant
n	Rotational speed [r/s]
n_p	Soil porosity
n_T	Rotation number [1/m]
n_c	Number of cutters
P_1	Resultant passive force in the central failure zone [N]
P_2	Resultant passive force in the side failure zone [N]
P_3	Normal pressure force on surface 3 [N]
P_4	Normal pressure force on surface 4 [N]
P_5	Normal pressure force on surface 5 [N]
P_6	Normal pressure force on surface 6 [N]
Pk	Half rotation
p_a	Atmospheric pressure [Pa]
p_{ref}	Reference stress [Pa]
Q_{TV}	Thrust [N]
q	Surcharge [Pa]
q_c	Cone resistance [Pa]
q_{cb}	Auger tip cone resistance [Pa]

q_{cnrm}	Normalized cone resistance [Pa]
q_{cs}	Auger shaft cone resistance [Pa]
q_t	Cone resistance corrected for pore pressure [Pa]
R_1	Soil reaction force in the central failure zone [N]
R_2	Soil reaction force in the side failure zone [N]
R_c	Friction ratio [%]
R_{cnrm}	Normalized friction ratio [%]
r	Average radius of auger flute [m]
r_1	Inner radius of drill bit [m]
r_2	Minor radius of auger flute [m]
r_3	Major radius of auger flute [m]
r_4	Outer radius of drill bit [m]
r_5	Radius of former cutters [m]
r_6	Radius of latter cutters [m]
s	Lead of auger [m]
T	Rotational torque [Nm]
T_a	Rotational torque of auger [Nm]
T_b	Rotational torque of drill bit [Nm]
t_{Tb}	Soil resistance under auger tip [Pa]
$t_{Ts;i}$	Soil resistance around auger section [Pa]
u_1	Pore pressure on the cone [Pa]
u_2	Pore pressure behind the cone [Pa]
u_3	Pore pressure behind the friction sleeve [Pa]
V_2	Force component in the vertical cutting direction [N]
V_b	Vertical cutter force [N]
$\boldsymbol{v}$	Penetration rate [m/s]
v_1	Cutting velocity [m/s]
$\boldsymbol{v}_a$	Absolute velocity of soil element [m/s]
$\boldsymbol{v}_{ez}$	Axial velocity of soil element [m/s]
$\boldsymbol{v}_{e\theta}$	Tangential velocity of soil element [m/s]
$\boldsymbol{v}_r$	Resultant velocity of soil element [m/s]
w	Width of cutter [m]
z	Penetration depth [m]

α	Helix angle of auger [rad]
α_1	Rake angle of cutter [rad]
β	Helix angle of soil element [rad]
β_1	Soil failure angle [rad]
γ	Angle between the direction of cutting and termination of the crescent [rad]
γ_s	Volumetric weight of soil [N/m^3]
γ_w	Volumetric weight of water [N/m^3]
Δu	Excess pore pressure [Pa]
δ	Skin friction angle [rad]
η_1	Coefficient of auger penetration depth
η_2	Coefficient of auger shape
η_3	Coefficient of subsoil stress level
η_4	Coefficient of auger penetration depth
θ	Rotation angle [rad]
λ	Rupture distance [m]
μ	Internal friction coefficient of soil
μ_1	Coefficient of friction between soil and drill tool
ρ	Soil density [kg/m^3]
σ_{v0}	Total overburden stress [Pa]
σ'_{v0}	Effective overburden stress [Pa]
ϕ'	Peak angle of friction [°]
φ	Internal friction angle of soil [rad]
$\boldsymbol{\omega}$	Angular velocity of auger [rad/s]
ω_1	Angular velocity of soil element [rad/s]

CFA	Continuous Flight Auger
CCFA	Cased Continuous Flight Auger
CPT	Cone Penetration Test
CPTu	Piezocone Penetration Test
DEM	Discrete Element Method
DTH	Down the Hole
FDP	Full Displacement Piling

FEM	Finite Element Method
MR	Mixed Reality
PFRT	Penetration Force and Rotational Torque
SCPTu	Seismic Piezocone Penetration Test
VR	Virtual Reality
WST	Weight Sounding Test

1 INTRODUCTION

Piling is a foundation engineering practice, where load transferring piles are planted deep in the ground to serve as support in soil conditions that are unfavorable for shallow foundations. Piles are generally divided into two categories depending on which type of load their carrying capacity is based on: bearing piles and friction piles. Bearing piles pass through poor material and penetrate a material with good bearing capacity, with the carrying capacity being dependent on point resistance. Friction piles generate their carrying capacity from the friction of the soil surrounding the pile, also known as skin friction. However, the total carrying capacity of both pile types is often a combination of both point resistance and skin friction. (Prakesh & Sharma 1990, p. 1)

The most common installation methods for piles include driving and drilling (Prakesh & Sharma 1990, p. 70). In this thesis, the focus is on installation by drilling. The main methods of drilling discussed will be CFA (Continuous Flight Auger) and FDP (Full Displacement Piling).

CFA process, shown in Figure 1, is a high-performance drilling technique, where the auger is drilled down to the final pile depth and the soil loosened by the auger tip is conveyed to the surface by the auger flight. The auger has a hollow stem, through which concrete is pumped while the auger is extracted. A possible reinforcement cage is then installed in the fresh concrete after auger extraction. A modified version of CFA called CCFA (Cased Continuous Flight Auger) also exists, which uses a casing outside of the auger. The casing prevents soft soil from mixing with the fresh concrete in unfavorable soil conditions. (BAUER Spezialtiefbau GmbH 2018, pp. 10–11)

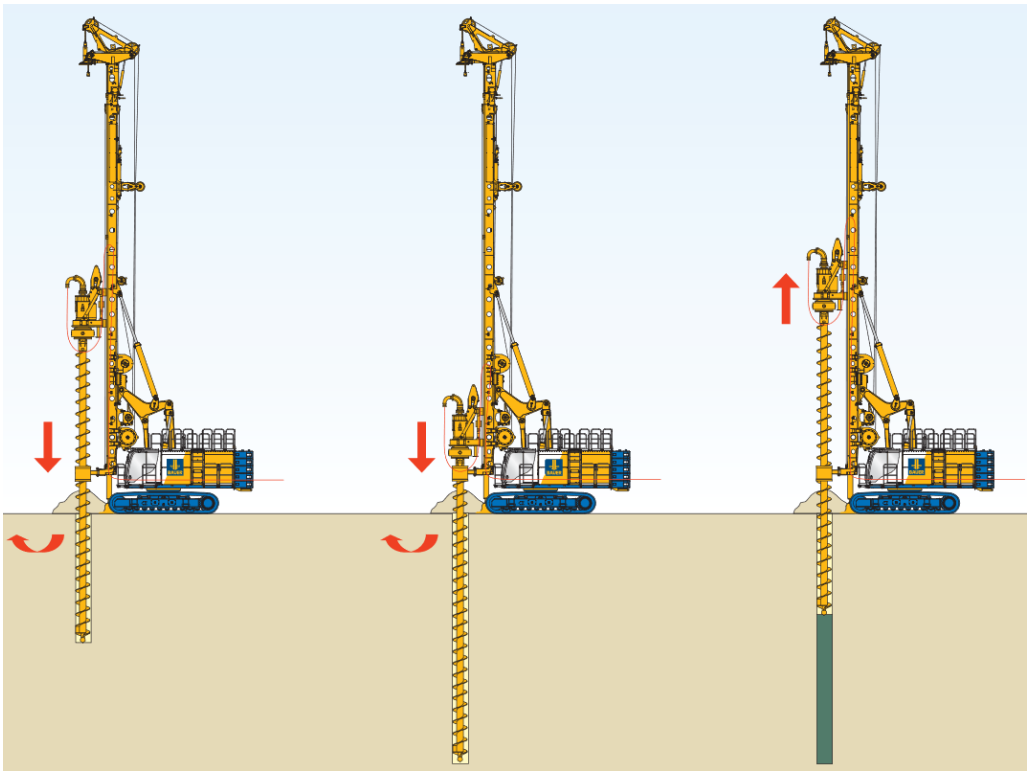

Figure 1. CFA process (BAUER Spezialtiefbau GmbH 2018, p. 10).

FDP is a method typically used in soft and displaceable soil conditions. The advantage FDP has over CFA is that very little loose soil is brought to the surface. Instead, the existing soil is laterally displaced and compacted during the drilling process by the thicker displacement body of the auger located above the starter bit. Concreting and reinforcement are done similarly to the CFA process, with the concrete being pumped through the hollow stem of the auger bit. The FDP process is shown in Figure 2. (BAUER Spezialtiefbau GmbH 2018, p. 12)

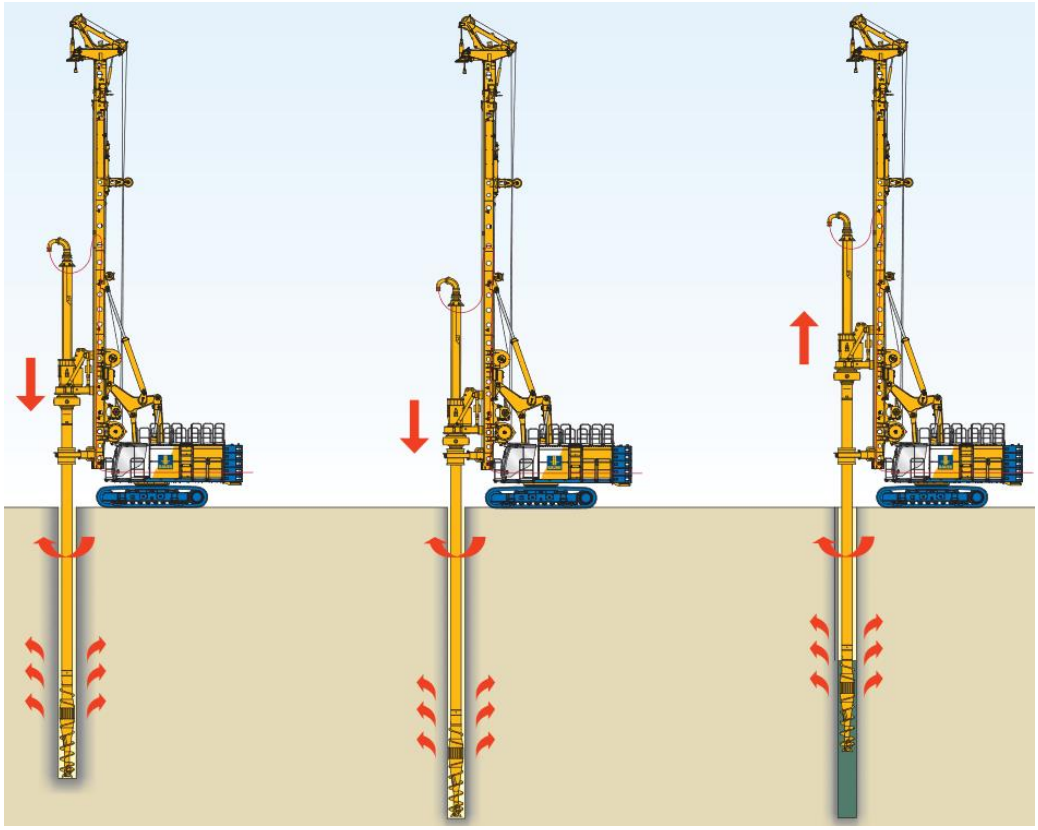

Figure 2. FDP process (BAUER Spezialtiefbau GmbH 2018, p. 12).

1.1 Background

Junttan Oy is a company founded in 1976 specializing in designing, manufacturing and marketing hydraulic piling equipment, based in Kuopio, Finland. Their product catalog includes mobile machines such as pile driving rigs and multipurpose drilling rigs, hydraulic impact hammers, power packs and rotary heads. Junttan also offers services such as rental equipment, training and technical support. (Junttan 2020a)

Junttan utilizes an MR (Mixed Reality) simulator running on Mevea software (Mevea Oy 2020a) for real-time simulation of a pile driving rig. The main target of the simulator is in product development, but it can also be used for rig operator training and marketing purposes at exhibitions. Using a simulator is especially efficient from the product development perspective, as for example control systems can be tested on a virtual platform without the need for building a prototype unit, which leads to significant cost savings and reduced development times. Currently, the simulator only has a model for a pile driving rig and there is a need to expand the simulator with models for other types of machines. The simulator is presented in Figure 3.

Figure 3. The Mixed Reality simulator.

The next goal is to develop a simulation model for multipurpose drilling rigs. The challenge however is that real soil is never homogenous, soil types change as depth increases. Accurate simulation requires modelling of multilayered soil since different types of soil cause different loading in the auger. Figure 4 shows an example of different soil layers.

Figure 4. Different soil layers (Fellenius 2018, p. 2-20).

1.2 Objectives

The main objective of this thesis is to develop a parametrized auger and layered soil simulation model for the MPx90 multipurpose drilling rig, shown in Figure 5, with a focus on CFA and FDP drilling methods. As the simulator is run in real-time, the model should fulfill the criteria of real-time simulation. This means achieving a loop duration of under 0.9 ms, which is the time step used in Mevea. High accuracy is not the goal for this model, but the results should be sufficiently realistic. The model will be simplified by assuming the borehole walls and drilling process to remain stable, so any extra loading such as the walls collapsing or the auger choking are ignored. Parametrization options for the soil should include the number of layers, layer depths and either the type of soil with pre-selected physical properties or user inputted values. For the auger, the user should be able to select the drilling method and the auger dimensions. The goal is to answer the following research questions:

- How could the auger and soil mechanics be simulated with a mathematical model that is suitable for the simulation environment and development of drilling rigs?
- How would the auger-soil system be implemented into a Mevea simulator in a way that achieves the goals for computational efficiency, functionality and realism?
- Which auger and soil properties need to be parametrized to allow the user to model different auger and soil types, and how to implement the parametrization?

Figure 5. MPx90 multipurpose drilling rig (Junttan 2020b).

This thesis consists of a literature review and an experimental part. The literature review focuses on examining the methods used for soil profiling, mechanics of CFA and FDP drilling and the available tools and methods for modelling the system. The experimental part focuses on implementing the information gained from the literature review to develop the simulation model. The experimental part also includes the validation of the model by comparing simulation results with measurement data obtained from a physical MPx90 unit.

2 METHODS

Following the literature review, the methods which were determined to be the most suitable for the auger models were selected. Both auger models are based on analytical methods. In the following chapters the software and auger models used in this thesis are presented. Methods for profiling soils and obtaining soil parameters are also presented.

2.1 Real-time simulation

The steady increase of computing power and its affordability in the past decades has led to the development of highly sophisticated simulation software applications, which allow the events in the simulation to occur on a natural time scale. This type of simulation, called real-time simulation, has become an important tool in a wide variety of engineering applications, examples of which include embedded system design, the control of dynamic processes and operator training (Damen Magazine 2017), (Normet 2020). Real-time simulation can also be used as a tool in solving sustainability issues. In the United States for example, power grid modifications for implementing renewable energy sources are tested in a virtual environment. VR (Virtual Reality) is recognized to be one of the key engineering challenges of the 21st century. For successful implementation of VR systems for human operators, the simulator must feel like it is part of the natural world. Receiving feedback in real time from virtual interface modules is essential for achieving this feeling. Development of these cyber-physical systems would not be possible without real-time simulation. (Popovici & Mosterman 2017, pp. ix-x)

2.2 Multibody dynamics

Multibody dynamics is a term used for the dynamic analysis of rigid and deformable components connected together. A multibody system is generally defined as a collection of subsystems, which are typically called bodies, components or substructures. These subsystems are connected to each other and kinematically constrained by different types of joints and their motion can be defined by translational and rotational displacements. Example of a multibody system is shown in Figure 6. The term rigid body refers to bodies where the deformations of the body are assumed to be so small that they have no effect on the general body motion. As such, the distance between any of the particles of a rigid body stays constant

at any time and configuration, meaning that the motion of the body can be expressed with only six generalized coordinates. Though computationally efficient, the resulting mathematical model is highly nonlinear due to the large body rotation. Deformable bodies on the other hand include the deformation of the body. To accurately model the deformation however, a large number of elastic coordinates may be required, which in turn requires more computing power. Neglecting body deformation may also be problematic, as this can lead to a mathematical model that fails to adequately present the actual system. Recently there has been an increased necessity to also include factors which have traditionally been ignored. This has largely been caused by a greater emphasis on the design of light and high-speed precision systems, some of which are operated in hostile environments. (Shabana 2005, pp. 1–2)

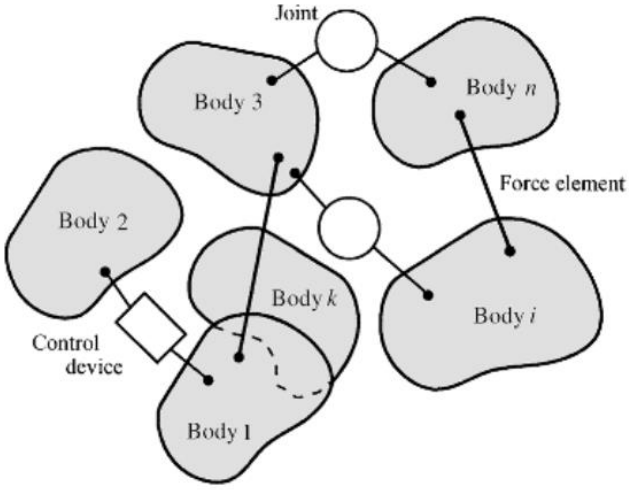

Figure 6. Multibody system (Shabana 2005, p. 3).

2.3 Continuous flight augering modelling

CFA is a complex process that has traditionally been simplified and modeled according to the operating principle of an Archimedean screw, due to the functional similarity between them. In recent years there has been a lot of research done on the subject, by for example Tian et al. (2015), Zhao et al. (2016) and Chen et al. (2018), in preparation for the Chinese Chang'e 5 lunar mission which aims to retrieve soil samples from the Moon. The CFA model used in this thesis will be based on the PFRT (Penetration Force and Rotational Torque) model proposed by Zhang & Ding (2016). The model developed by Zhang & Ding uses a drill tool consisting of a double helix auger and a drill bit with cutters for breaking the soil,

as shown in Figure 7. This model was chosen as the basis since it includes the same modelling principle as other auger models and a drill bit, which may be equipped on some augers.

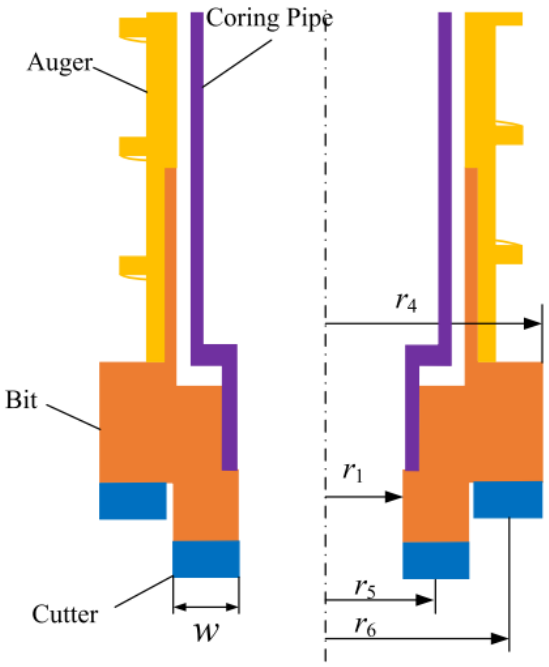

Figure 7. Auger with a drill bit (Zhang & Ding 2016, p. 191).

The model is based on quasi-static Mohr-Coulomb soil mechanics and the total loading during the drilling process is obtained from the sum of loads on the drill bit and the auger. In this model, the loading in the auger is caused by the conveyance mechanism of the auger flights. As the auger penetrates deeper into the soil and soil cuttings are transported along the auger, the relative motion between the soil and auger causes frictional forces on the surfaces of auger, which are the main cause of loading. This model assumes the soil to be conveyed at a steady state. The motion of a soil element in the auger flights is presented in Figure 8 and Figure 9. The element is placed in a cylindrical coordinate system where it rotates around the axis of rotation, penetration depth z, in an angle θ. (Zhang & Ding 2016, p. 192)

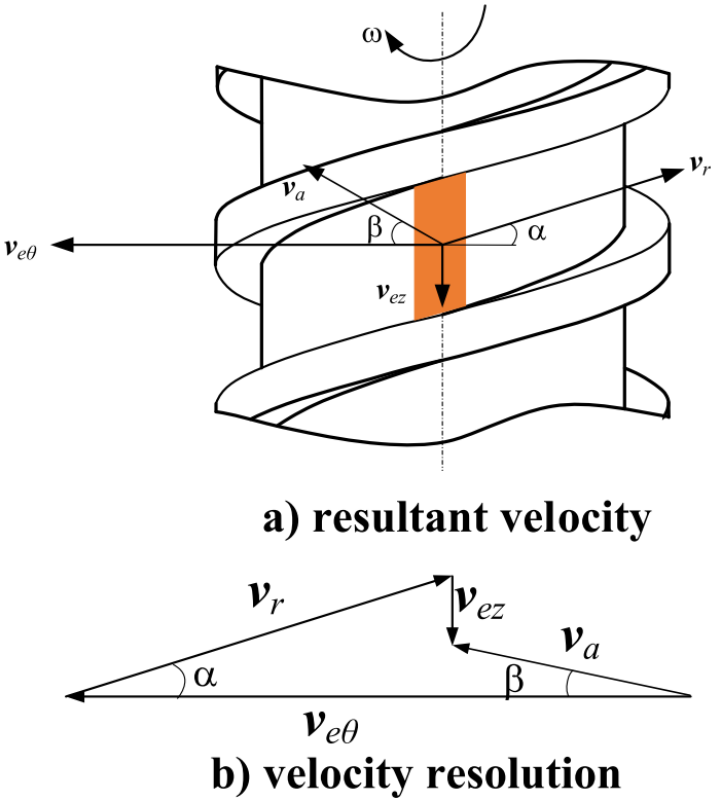

Figure 8. Motion analysis of a soil element (Zhang & Ding 2016, p. 193).

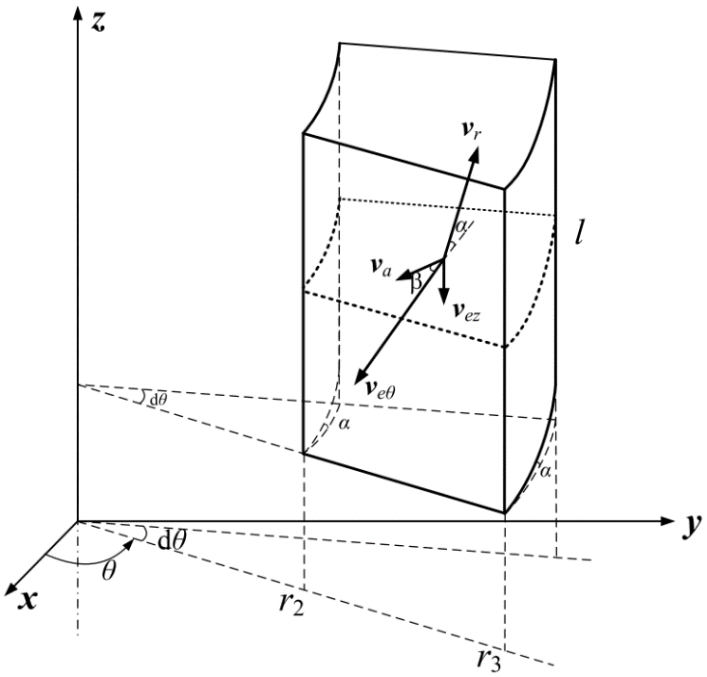

Figure 9. Velocity stereogram of a soil element (Zhang & Ding 2016, p. 193).

The relationships of the soil element velocity components can be expressed as follows:

$$\boldsymbol{v}_{\mathrm{a}} = \boldsymbol{v}_{\mathrm{r}} + \boldsymbol{v}_{\mathrm{e\theta}} + \boldsymbol{v}_{\mathrm{ez}} \tag{1}$$

$$v_{\mathrm{r}} \sin(\alpha) - v_{\mathrm{ez}} = v_{\mathrm{a}} \sin(\beta) \tag{2}$$

$$\omega_1 r - v_{\mathrm{r}} \cos(\alpha) = v_{\mathrm{a}} \cos(\beta) \tag{3}$$

where $\boldsymbol{v}_{\mathrm{a}}$ is the absolute velocity, $\boldsymbol{v}_{\mathrm{r}}$ is the relative velocity, $\boldsymbol{v}_{\mathrm{e\theta}}$ is the tangential velocity, $\boldsymbol{v}_{\mathrm{ez}}$ is the axial velocity, α is the helix angle of the auger, β is the helix angle of the soil element, ω_1 is the angular velocity of the soil element and r is the average radius of the auger flute (Zhang & Ding 2016, pp. 193–194).

The velocity components $\boldsymbol{v}_{\mathrm{ez}}$ and $\boldsymbol{v}_{\mathrm{e\theta}}$ are dependent on the motion of the auger and are given as:

$$\boldsymbol{v}_{\mathrm{ez}} = \boldsymbol{v} \tag{4}$$

$$\boldsymbol{v}_{\mathrm{e\theta}} = \boldsymbol{\omega} \times \boldsymbol{r} \tag{5}$$

where $\boldsymbol{v}$ is the penetration rate and $\boldsymbol{\omega}$ is the angular velocity of the auger (Zhang & Ding 2016, p. 193).

The amount of removed cuttings is assumed to be equal to the amount of cuttings generated according to the equal-volume principle. Thus, this relationship can be described by the following equation:

$$v\pi(r_4^2 - r_1^2) = 2v_{\mathrm{r}} l \cos(\alpha)(r_3 - r_2) \tag{6}$$

where r_4 is the outer radius of drill bit, r_1 is the inner radius of drill bit, l is the auger flute width, r_3 is the major radius of auger flute and r_2 is the minor radius of auger flute (Zhang & Ding 2016, p. 194).

For the force analysis, a soil element in the auger flute with a central angle $d\theta$ and height equal to the flute width l as seen in Figure 10 is inspected. The element has pressure forces acting on all its six surfaces. As the element is assumed to be conveyed in a steady state, no relative motion exists on the element's rear and front surfaces. This means that there are no friction forces on these surfaces. The pressure forces on the upper and lower surfaces and the surface facing the auger stem cause friction forces in the opposite direction of $\boldsymbol{v}_r$, while the friction force between the soil element and borehole wall acts in the opposite direction of $\boldsymbol{v}_a$. The soil element is also affected by its own weight and a centrifugal force. The upper and lower surfaces are called surfaces 1 and 2 respectively, the surface facing the borehole wall is surface 3, the surface facing the auger stem is surface 4 and the front and rear surfaces are surfaces 6 and 5, respectively. (Zhang & Ding 2016, p. 194)

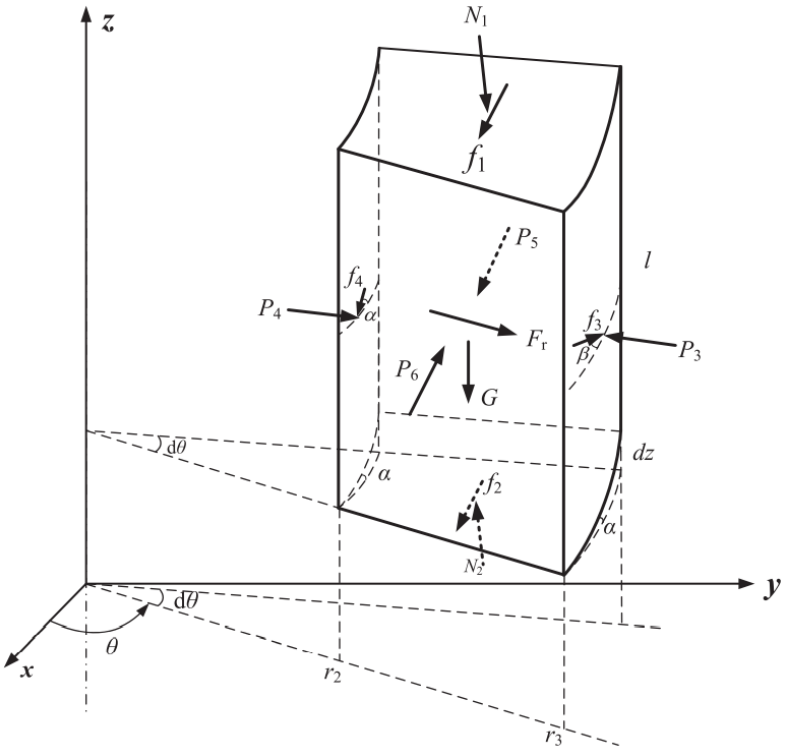

Figure 10. Force analysis of a soil element (Zhang & Ding 2016, p. 193).

The equilibrium equations of the soil element can be obtained as:

$$\sum F_y = P_4 - P_3 + F_r = 0 \tag{7}$$

$$\sum F_z = (N_2 - N_1)\cos(\alpha) - G - (f_1 + f_2 + f_4)\sin(\alpha) - f_3 \sin(\beta) = 0 \tag{8}$$

$$\sum F_x = P_6 - P_5 - (f_1 + f_2 + f_4)\cos(\alpha) + (N_1 - N_2)\sin(\alpha) + f_3\cos(\beta) = 0 \quad (9)$$

where P_4 is the normal pressure force on surface 4, P_3 is the normal pressure force on surface 3, F_r is the centrifugal force, N_2 is the normal pressure force on surface 2, N_1 is the normal pressure force on surface 1, G is the soil element's weight, P_6 is the normal pressure force on surface 6, P_5 is the normal pressure force on surface 5 and f_1, f_2, f_3 and f_4 are the friction forces caused by N_1, N_2, P_3 and P_4 respectively. (Zhang & Ding 2016, p. 194)

The friction forces can be calculated as (Zhang & Ding 2016, p. 191):

$$f_1 = \mu_1 N_1 \quad (10)$$

$$f_2 = \mu_1 N_2 \quad (11)$$

$$f_3 = \mu P_3 \quad (12)$$

$$f_4 = \mu_1 P_4 \quad (13)$$

where μ is the internal friction coefficient of soil and μ_1 is the friction coefficient between soil and auger.

The soil is assumed to be in a state of plastic equilibrium and to have internal friction and be homogenous and isotropic. As such, according to Rankine's active soil pressure theory forces P_6, P_5 and P_3 can be calculated as:

$$P_3 = \frac{1}{4} K_0 \rho g r_3 l(Nz + l) d\theta \quad (14)$$

$$P_5 = \frac{1}{2} K_0 \rho g l(r_3 - r_2)(Nz + l) \quad (15)$$

$$P_6 = \frac{1}{2} K_0 \rho g l(r_3 - r_2)(Nz + l + Ndz) \quad (16)$$

where K_0 is the coefficient of active earth pressure, ρ is soil density, N is the number of auger helices and g is gravitational acceleration. (Zhang & Ding 2016, p. 194)

The angle θ is related to the penetration depth z and this relation can be expressed as (Zhang & Ding 2016, p. 194):

$$dz = \frac{s}{2\pi} d\theta \tag{17}$$

where s is the lead of auger.

According to the Mohr-Coulomb failure criterion, the coefficient of active earth pressure can be approximated by the equation (Verrujit 2018, p. 251):

$$K_0 = \frac{1-\sin(\varphi)}{1+\sin(\varphi)} \tag{18}$$

where φ is the internal friction angle of soil.

Finally, soil element weight and the centrifugal force can be calculated as (Zhang & Ding 2016, p. 194):

$$G = \frac{1}{2}\rho g l(r_3^2 - r_2^2)d\theta \tag{19}$$

$$F_r = \frac{1}{2}\rho\omega_1^2 r l(r_3^2 - r_2^2)d\theta \tag{20}$$

Planar force diagram of the forces affecting a soil element in the auger flute is presented in Figure 11. To calculate the force and torque in the auger, the forces exerted on the auger are required. According to Figure 11, the forces acting on the auger are N_1, f_1, f_4, N_2 and f_2. As the drilling conditions were assumed to be non-choking, there is no pressure on the top surface of the soil element and forces N_1 and f_1 are assumed to be zero. The penetration force and rotational torque of the auger can then be calculated as (Zhang & Ding 2016, p. 194):

$$F_{\mathrm{a}} = \int_0^z (f_2 \sin(\alpha) - N_2 \cos(\alpha) + f_4 \sin(\alpha)) \tag{21}$$

$$T_{\mathrm{a}} = \int_0^z (f_2 \cos(\alpha)\, r + N_2 \sin(\alpha) r + f_4 \cos(\alpha) r_2) \tag{22}$$

where F_{a} is the penetration force of the auger and T_{a} is the rotational torque of the auger.

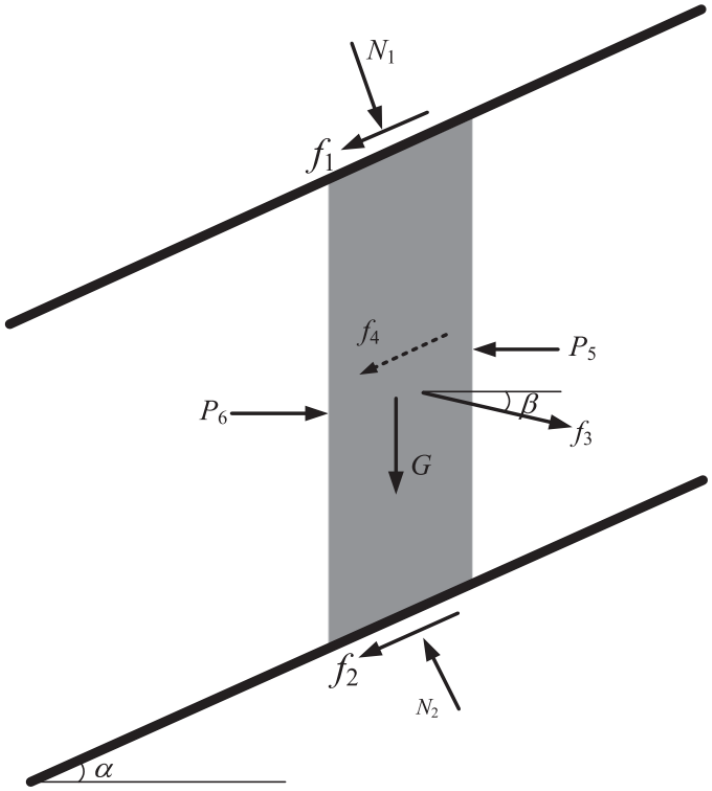

Figure 11. Planar force diagram of a soil element (Zhang & Ding 2016, p. 193).

If the auger has an additional drill bit for cutting the soil, the force and torque generated by it must also be considered. Like the auger model presented above, the commonly used approach for predicting soil-cutter forces is based on quasi-static Mohr-Coulomb soil mechanics and utilizes methods developed by Reece (1964) and McKyes & Ali (1977). In this approach, the three-dimensional soil failure is considered to consist of a center wedge failure and side crescent failures, as shown in Figure 12. This method has traditionally been favored due to the computational speed and simplicity it offers. (Zhang & Ding 2016, p. 194)

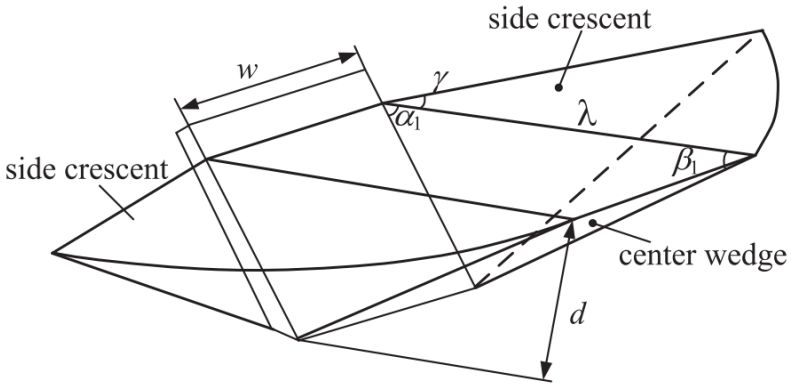

Figure 12. Soil-cutter failure zone (Zhang & Ding 2016, p. 193).

Center wedge failure, which consists of a plane failure occurring in the central failure zone, is presented in Figure 13. Assuming that the soil is homogenous and isotropic, the force equilibrium equations can be expressed as:

$$P_1 \sin(\alpha_1 + \delta) + c_a w d \cot(\alpha_1) = R_1 \sin(\beta_1 + \varphi) + cdw\cot(\beta_1) + \frac{1}{2}\lambda dw\rho a \quad (23)$$

$$P_1 \cos(\alpha_1 + \delta) - c_a w d = -R_1 \cos(\beta_1 + \varphi) + cwd + q\lambda w + \frac{1}{2}\lambda d\rho g w \quad (24)$$

where P_1 is the resultant passive force in the central failure zone, α_1 is the rake angle of cutter, δ is the skin friction angle, c_a is the adhesion between soil and drill bit, w is the width of cutter, d is cut per revolution v/n where n is rotational speed, R_1 is the soil reaction force in the central failure zone, β_1 is the soil failure angle, c is the cohesion of soil, λ is the rupture distance, a is the acceleration of soil being cut and q is surcharge. (Zhang & Ding 2016, p. 194)

As velocity increases from zero at B to v_1 at A at a constant acceleration, the soil acceleration can be calculated as (Zhang & Ding 2016, p. 194):

$$a = \frac{2v_1^2}{d}\frac{\sin(\alpha_1)\sin(\beta_1)}{\sin(\alpha_1+\beta_1)} \quad (25)$$

where v_1 is the cutting velocity, which can be calculated from (Zhang & Ding 2016, p. 191):

$$v_1 = \omega_1 r_5 \tag{26}$$

$$v_1 = \omega_1 r_6 \tag{27}$$

where r_5 is the radius of former cutters and r_6 is the radius of latter cutters.

Soil failure angle β_1 can be obtained using Rankine's passive earth pressure theory as (Verrujit 2018, p. 254):

$$\beta_1 = \frac{\pi}{4} - \frac{\varphi}{2} \tag{28}$$

Surcharge q can be calculated as (Zhang & Ding 2016, p. 191):

$$q = \rho g z \tag{29}$$

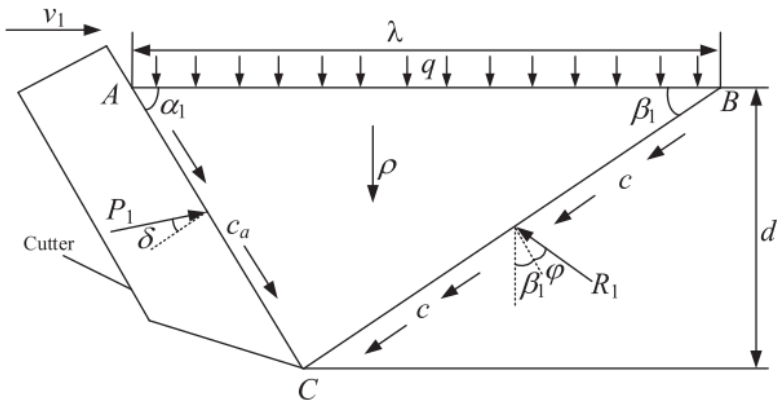

Figure 13. Force diagram of the central failure zone (Zhang & Ding 2016, p. 194).

Force P_1 can be obtained from Reece's fundamental earth-moving equation as (Reece 1964, p. 18):

$$P_1 = \rho g d^2 N_{\rho 1} + c d N_{c1} + q d N_{q1} + c_a d N_{ca1} \tag{30}$$

The weakness with this equation however is that it considers the tool movement to be purely horizontal and does not consider the vertical velocity present in drilling operations. A

modified version of this equation which includes vertical velocity can be expressed in the form of (Zhang & Ding 2016, p. 195):

$$P_1 = \rho g d^2 N_{\rho 1} + c d N_{c1} + q d N_{q1} + c_a d N_{ca1} + \rho v^2 d N_{a1} \tag{31}$$

where $N_{\rho 1}$, N_{c1}, N_{q1}, N_{ca1} and N_{a1} are constants which can be calculated as:

$$N_{\rho 1} = \frac{\sin(\alpha_1+\beta_1)\sin(\beta_1+\varphi)}{2\sin(\alpha_1)\sin(\beta_1)\sin(\alpha_1+\delta+\beta_1+\varphi)} w \tag{32}$$

$$N_{c1} = \frac{\cos(\varphi)}{\sin(\beta_1)\sin(\alpha_1+\delta+\beta_1+\varphi)} w \tag{33}$$

$$N_{q1} = \frac{\sin(\alpha_1+\beta_1)\sin(\beta_1+\varphi)}{\sin(\alpha_1)\sin(\beta_1)\sin(\alpha_1+\delta+\beta_1+\varphi)} w \tag{34}$$

$$N_{ca1} = -\frac{\cos(\alpha_1+\beta_1+\varphi)}{\sin(\alpha_1)\sin(\alpha_1+\delta+\beta_1+\varphi)} w \tag{35}$$

$$N_{a1} = \frac{\cos(\beta_1+\varphi)}{\sin(\alpha_1+\delta+\beta_1+\varphi)} w \tag{36}$$

Side crescent failure zone is presented in Figure 14. Sector element $d\gamma$ of the angle γ between the direction of cutting and the termination of the curved section of the crescent is inspected for force analysis. The force equilibrium equations can be expressed as (McKyes & Ali 1977, p. 47):

$$dP_2 \sin(\alpha_1 + \delta) = dR_2 \sin(\beta_1 + \varphi) + \frac{c\lambda d\cos(\beta_1) d\gamma}{2\sin(\beta_1)} \tag{37}$$

$$dP_2 \cos(\alpha_1 + \delta) + dR_2 \cos(\beta_1 + \varphi) = \frac{1}{6}\rho g d\lambda^2 d\gamma + \frac{1}{2} c d\lambda d\gamma + \frac{1}{2} q\lambda^2 d\gamma \tag{38}$$

where P_2 is the resultant passive force in the side failure zone and R_2 is the soil reaction force in the side failure zone. An approximated solution for the angle γ has been developed by Godwin & Spoor (1977, p. 217), which can be expressed in the form of (Zhang & Ding 2016, p. 195):

$$\gamma = \cos^{-1}\left(\frac{\sin(\beta_1)\cos(\alpha_1)}{d\sin(\alpha_1+\beta_1)}\right) \tag{39}$$

The horizontal and vertical force components in the cutters can then be obtained as follows (McKyes & Ali 1977, p. 47):

$$dH_2 = dP_2 \sin(\alpha_1 + \delta)\cos(\gamma) \tag{40}$$

$$dV_2 = dP_2 \cos(\alpha_1 + \delta) \tag{41}$$

where H_2 is the force component in the horizontal cutting direction and V_2 is the force component in the vertical cutting direction. The total horizontal and vertical forces are thus (Zhang & Ding 2016, p. 195):

$$H_2 = \int_0^{\gamma} dP_2 \sin(\alpha_1 + \delta)\cos(\gamma) = \rho g d^2 N_{\rho 2} + cdN_{c2} + qdN_{q2} \tag{42}$$

$$V_2 = \int_0^{\gamma} dP_2 \cos(\alpha_1 + \delta) = \rho g d^2 N_{\rho 3} + cdN_{c3} + qdN_{q3} \tag{43}$$

where $N_{\rho 2}$, N_{c2}, N_{q2}, $N_{\rho 3}$, N_{c3}, N_{q3} are constants which can be obtained from:

$$N_{\rho 2} = \frac{\sin(\alpha_1+\delta)\sin(\beta_1+\varphi)\sin^2(\alpha_1+\beta_1)}{6\sin(\alpha_1+\delta+\beta_1+\varphi)\sin^2(\alpha_1)\sin^2(\beta_1)}\sin(\gamma d) \tag{44}$$

$$N_{c2} = \frac{\sin(\alpha_1+\delta)\sin(\alpha_1+\beta_1)\cos(\varphi)}{2\sin(\alpha_1+\delta+\beta_1+\varphi)\sin^2(\alpha_1)\sin^2(\beta_1)}\sin(\gamma d) \tag{45}$$

$$N_{q2} = \frac{\sin(\alpha_1+\delta)\sin(\beta_1+\varphi)\sin^2(\alpha_1+\beta_1)}{2\sin(\alpha_1+\delta+\beta_1+\varphi)\sin^2(\alpha_1)\sin^2(\beta_1)}\sin(\gamma d) \tag{46}$$

$$N_{\rho 3} = \frac{\sin(\alpha_1+\delta)\sin(\beta_1+\varphi)\sin^2(\alpha_1+\beta_1)}{6\sin(\alpha_1+\delta+\beta_1+\varphi)\sin^2(\alpha_1)\sin^2(\beta_1)}\gamma d \tag{47}$$

$$N_{c3} = \frac{\sin(\alpha_1+\delta)\sin(\alpha_1+\beta_1)\cos(\varphi)}{2\sin(\alpha_1+\delta+\beta_1+\varphi)\sin^2(\alpha_1)\sin^2(\beta_1)}\gamma d \tag{48}$$

$$N_{q3} = \frac{\sin(\alpha_1+\delta)\sin(\beta_1+\varphi)\sin^2(\alpha_1+\beta_1)}{2\sin(\alpha_1+\delta+\beta_1+\varphi)\sin^2(\alpha_1)\sin^2(\beta_1)}\gamma d \tag{49}$$

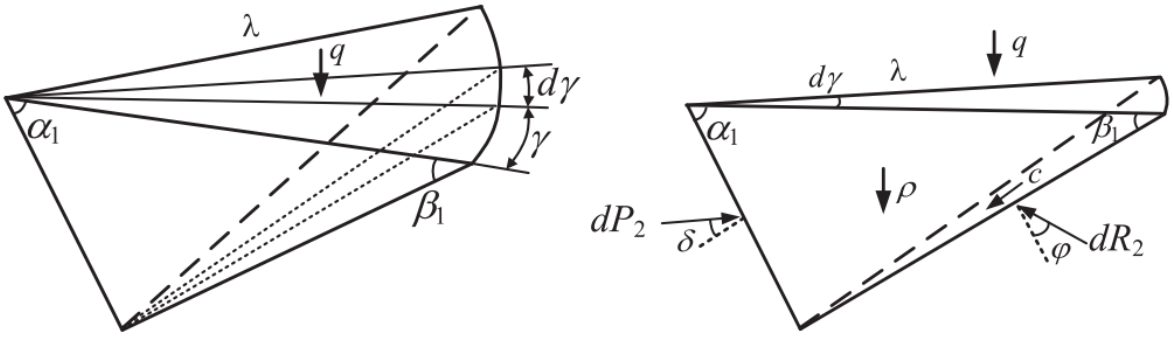

Figure 14. Force diagram of the side crescent failure zone (Zhang & Ding 2016, p. 194).

The total horizontal and vertical forces in one cutter are a result of the forces in the central and two side failure zones and the soil-bit interface adhesion. The horizontal and vertical forces on one cutter can be calculated as (Godwin & Spoor 1977, p. 219):

$$H_b = P_1 \sin(\alpha_1 + \delta) + 2H_2 + c_a w d \cos(\alpha_1) \tag{50}$$

$$V_b = -P_1 \cos(\alpha_1 + \delta) + 2V_2 + c_a w d \sin(\alpha_1) \tag{51}$$

where H_b is the horizontal cutter force and V_b is the vertical cutter force.

The total penetration force in the drill bit is the result of the sum of vertical cutter forces and the force exerted by the soil surcharge. The total torque in the drill bit is the result of the sum of horizontal cutter forces. The drill bit penetration force and rotational torque are (Zhang & Ding 2016, p. 195):

$$F_b = n_c V_b + \pi r_4^2 q \tag{52}$$

$$T_b = \frac{n_c}{2}(r_5 + r_6) H_b \tag{53}$$

where F_b is the penetration force of the drill bit, T_b is the rotational torque of the drill bit and n_c is the number of cutters.

In the PFRT model, the total loading during the drilling process is a sum of the loads in the auger and the drill bit. The total penetration force and rotational torque can then be expressed as (Zhang & Ding 2016, p. 195):

$$F = F_{\mathrm{a}} + F_{\mathrm{b}} \tag{54}$$

$$T = T_{\mathrm{a}} + T_{\mathrm{b}} \tag{55}$$

where F is the penetration force and T is the rotational torque.

If the auger does not use a drill bit, the penetration force at the tip can be calculated using the soil surcharge term used in equation 52. Another way is by using a similar method as in FDP modelling, shown in the following chapter.

2.4 Full displacement piling modelling

Much of the previous research on FDP process loading has been based on FEM (Finite Element Method) and DEM (Discrete Element Method) analysis, such as Pucker & Grabe (2012), Krasiński (2014) and Shi et al. (2019). Although these methods would provide sufficiently accurate results, they are computationally heavy, and the simulation speed requirement would probably not be achieved. Instead, two possible methods for FDP modelling are proposed: one based on research done by Krasiński (2015) and the other based on the PFRT model presented above.

The model developed by Krasiński uses a simplified scheme of the auger to calculate the torque and thrust during the FDP process using cone resistance q_{c} obtained from CPT (Cone Penetration Test) testing. In this model, the FDP auger is divided into four sections: the tip with a constant stem diameter, the section with an increasing stem diameter after the tip, the displacement part and the helix following the displacement part, as shown in Figure 15.

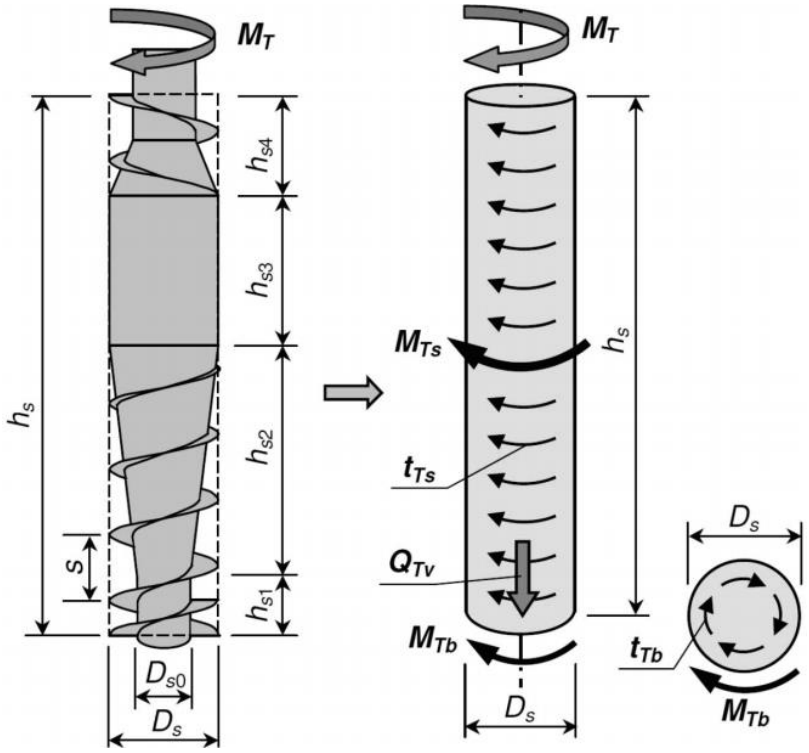

Figure 15. Simplified scheme of FDP auger (Krasiński 2015, p. 50).

The total torque is a sum of torques caused by the friction around the auger shaft and the auger tip, as described by the following equation (Krasiński 2015, p. 50):

$$M_{\mathrm{T}} = M_{\mathrm{Ts}} + M_{\mathrm{Tb}} \tag{56}$$

where M_{T} is the total torque, M_{Ts} is the torque in the auger shaft and M_{Tb} is the torque in the auger tip. The torque components are calculated as (Krasiński 2015, p. 50):

$$M_{\mathrm{Ts}} = \frac{\pi D_{\mathrm{s}}^2}{2} \sum t_{\mathrm{Ts;i}} h_{\mathrm{s;i}} \tag{57}$$

$$M_{\mathrm{Tb}} = \frac{\pi D_{\mathrm{s}}^3}{12} t_{\mathrm{Tb}} \tag{58}$$

where D_{s} is the diameter of the displacement part, $h_{\mathrm{Ts;i}}$ is the length of an auger section i, $t_{\mathrm{Ts;i}}$ is the soil resistance around auger section i and t_{Tb} is the soil resistance at the auger tip.

Soil resistances t_{Ts} and t_{Tb} can be acquired from equations (Krasiński 2015, p. 55):

$$t_{\mathrm{Ts}} = 0.035\eta_1\eta_2\eta_3 q_{\mathrm{cs}} \tag{59}$$

$$t_{\mathrm{Tb}} = 1.2\eta_3\eta_4 m_{\mathrm{Ts}} \frac{q_{\mathrm{cb}}}{n_{\mathrm{T}}} \tag{60}$$

where η_1 and η_4 are coefficients dependent on the penetration depth, η_2 is the coefficient of auger shape influence which is related to D_s and minimum auger shaft diameter D_{s0}, η_3 is the coefficient of subsoil stress level, q_{cs} is the cone resistance of the shaft section, q_{cb} is the cone resistance in the auger tip, n_T is the number of rotations per penetration depth and m_{Ts} is a coefficient dependent on shaft torque obtained from formula (Krasiński 2015, p. 53):

$$m_{\mathrm{Ts}} = \frac{M_{\mathrm{Ts}}}{sD_s^2 p_{\mathrm{ref}}} \tag{61}$$

where p_{ref} is reference stress of 1.0 MPa.

Cone resistance q_{cs} can be obtained as an average of q_c along the auger length h_s and q_{cb} can be obtained from the average of q_c from -D_s to +D_s around the auger base level (Krasiński 2015, p. 52). Coefficients η_1, η_2 and η_4 are empiric coefficients, which can be acquired from Figure 16.

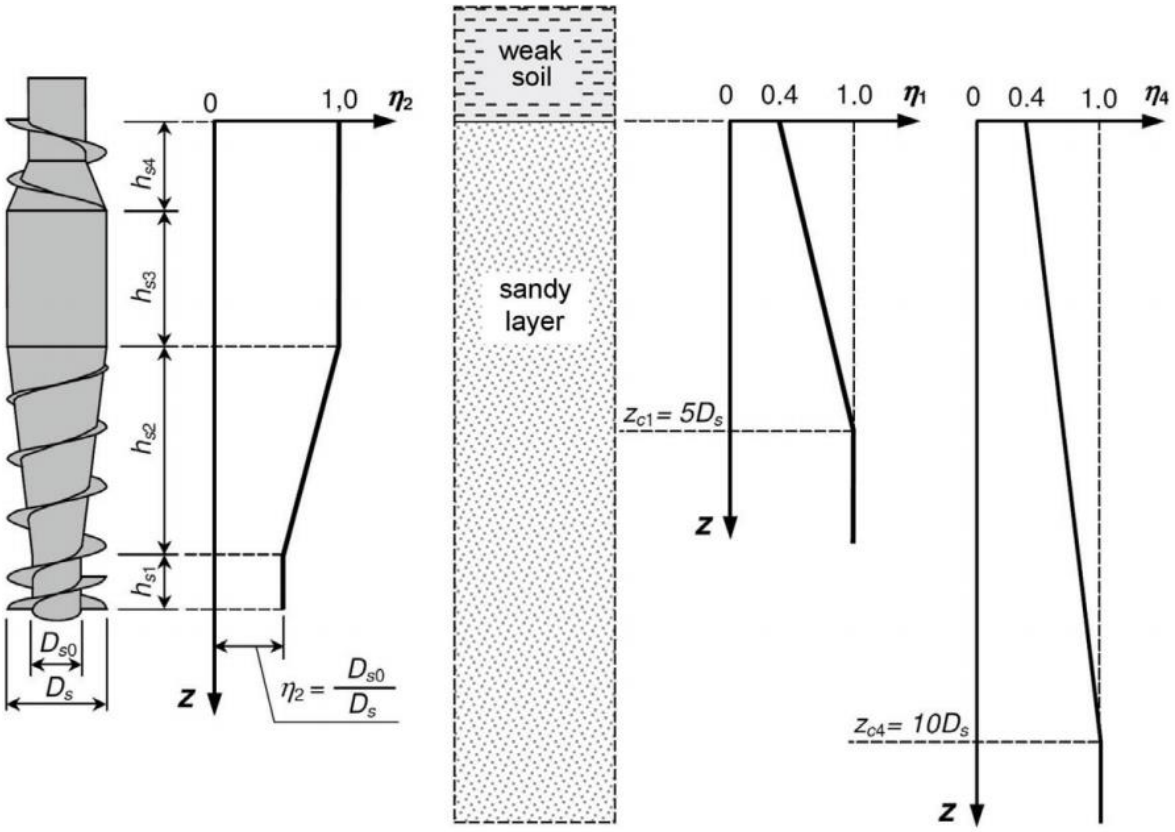

Figure 16. Diagrams for determining coefficients η_1, η_2 and η_4 (Krasiński 2015, p. 54).

Coefficient η_3 considers the stress level in the subsoil and can be expressed as (Krasiński 2015, p. 55):

$$\eta_3 = \frac{\sigma'_{v0}}{100\ \text{kPa}} \tag{62}$$

where σ'_{v0} is the effective overburden stress in the subsoil, which, according to Terzaghi's stress effective principle, can be calculated from (Verrujit 2018, p. 40):

$$\sigma'_{vo} = (\gamma_s - \gamma_w)z \tag{63}$$

where γ_s is the volumetric weight of soil and γ_w is the volumetric weight of water, which is usually 10 kN/m^3. Volumetric weight of soil can be expressed as (Verrujit 2018, p. 25):

$$\gamma_s = (1 - n_p)\rho g \tag{64}$$

where n_p is the porosity of the soil. Theoretically the value of n_p can range from 0.25 to 0.45 and for most soils the range is from 0.30 to 0.45, with a lower value indicating a denser soil and vice versa (Verrujit 2018, pp. 21–22).

According to the principles of screw operation and energy conservation, there exists a relation between auger torque and thrust. The thrust during the FDP process can be calculated from:

$$Q_{Tv} = a_r \frac{2\pi M_{Ts}}{n_T s} \tag{65}$$

where a_r is a reduction factor, which takes into account the loss caused by soil friction and the lower penetration velocity than what the helix of the auger would cause. The value of a_r is lower than 1, but the exact value is unknown. (Krasiński 2015, p. 53)

The alternative method of modelling the FDP process is by using a similar method as in the CFA process. This can be accomplished by dividing the auger into different sections, just like in the FDP model described above. The loading is assumed to result from soil friction in the auger flights and the friction of the displacement part and the borehole wall. The changing diameter of the auger stem would have to be included in the equations. The downside of using the PFRT model is that it does not consider the radial stresses occurring due to soil displacement and would potentially prove to be too inaccurate. Just as the CFA model can be utilized in the FDP process, parts of the FDP model can be used in the CFA model. Most importantly in the case of a CFA auger without a drill bit, the torque and force at the tip can be calculated using equations 58 and 65.

2.5 Soil profiling

For the proper simulation of drilling in a multilayer soil, information about the soil types and soil profile are required. The CFA model also requires density and friction angle parameters for each layer. Typical values for soil types can be used for both parameters, though different soil testing methods can also be used to calculate them. Suitability of the most common in-situ tests for geotechnical parameters are presented in Figure 17. According to the table, CPT and its derivatives are the most suitable for all the required soil characteristics. As the

presented FDP model also requires CPT data, this chapter will focus on cone penetration testing.

Group	In-situ Test	Geotechnical Parameter												Ground Type					
		Soil type	Profile	u_0	OCR	D_R-ψ	ϕ'	s_u	G_o - E	σ–ε	M - C_c	k	c_v	hard rock	soft rock	gravel	sand	silt/clay	peat – organic
Penetrometer/ Direct Push	Dy. Probing (DP)	C	B	-	C	C	C	C	C	-	-	-	-	-	C	B	A	B	B
	SPT	B	B	-	C	B	C	C	C	-	-	-	-	-	C	B	A	B	B
	CPT	B	A	-	B	B	B	B	B	C	C	C	-	-	B	B	A	A	A
	CPTu	A	A	A	B	A	B	A	B	C	B	A	A	-	B	B	A	A	A
	SCPTu	A	A	A	A	A	B	A	A	B	B	A	A	-	B	B	A	A	A
	DMT	B	B	B	B	C	B	B	B	C	B	C	B	-	C	C	A	A	A
	SDMT	B	B	B	A	B	B	B	A	B	B	C	B	-	C	C	A	A	A
	Full-flow (T/ball)	C	B	B	B	C	C	A	C	C	C	C	C	-	-	-	C	B	A
	Field vane (FVT)	B	C	-	B	-	-	A	-	-	-	-	-	-	-	-	-	A	B
Pressuremeter	Pre-bored	B	B	-	C	C	C	B	B	C	C	-	C	A	A	B	B	B	B
	Self-bored	B	B	A[1]	B	B	B	B	A	A	B	B	A[1]	-	C	-	B	A	B
	Full-displacement	B	B	B	C	C	C	B	A	A	B	B	A	-	C	-	B	A	A
Other	Screw/plate load	C	-	-	B	C	C	B	B	B	B	C	C	C	A	B	B	B	B
	Borehole shear	C	-	-	-	-	B	C	-	-	-	-	-	C	B	C	C	C	-
	Permeameter	C	-	A	-	-	-	-	-	-	-	A	B	A	A	A	A	A	B
	Borehole seismic	C	C	-	B	C	-	-	A	C	-	-	-	A	A	A	A	A	B
	Surface seismic	-	C	-	B	C	-	-	A	C	-	-	-	A	A	A	A	A	A
	Hydraulic fracture	-	-	B	-	-	-	-	-	-	-	C	C	B	B	-	-	B	C

Applicability: A = high, B = moderate, C = low, - = none

Figure 17. Applicability of common in-situ tests for geotechnical parameters and ground types (Robertson & Cabal 2012, p. 3).

CPT is a process in which a cone on the end of series of rods is pushed into the ground at a constant rate. The process is one of the most popular methods for profiling soils and is the only method that uses continuous sampling. During the process, resistance to the cone penetration is measured at continuous or intermittent intervals. Measurements can be made of either the combined cone penetration resistance and outer surface of a sleeve or the resistance of a surface sleeve. Cone resistance q_c is obtained by dividing the measured force acting on the cone by the projected area of the cone. Sleeve friction f_s is obtained by dividing the measured force acting on the friction sleeve by the surface area of the friction sleeve. CPTu (Piezocone Penetration Test), commonly called the piezocone test, also measures pore pressure at one to three locations. These pore pressures are marked as: u_1 on the cone, u_2 on the cone shoulder and u_3 behind the friction sleeve, as shown in Figure 18. Soil profile obtained from CPTu data can be seen in Figure 19. (Lunne et al. 1997, pp. 1–2)

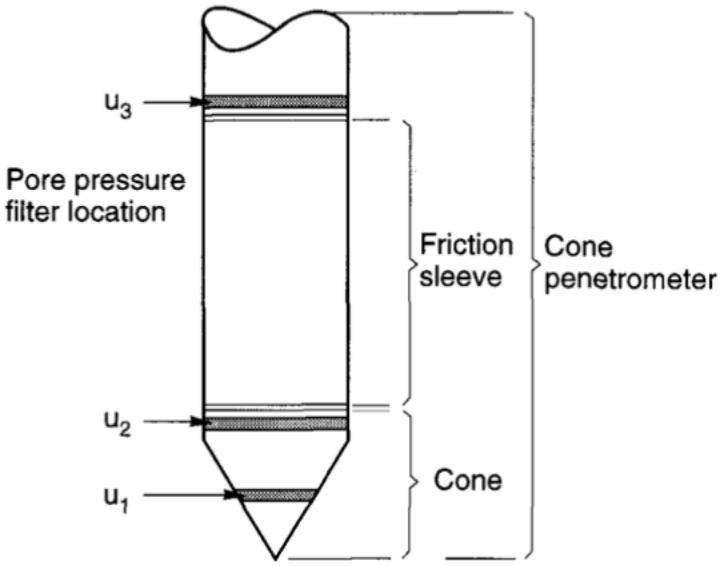

Figure 18. CPTu cone penetrometer structure (Lunne et al. 1997, p. 2).

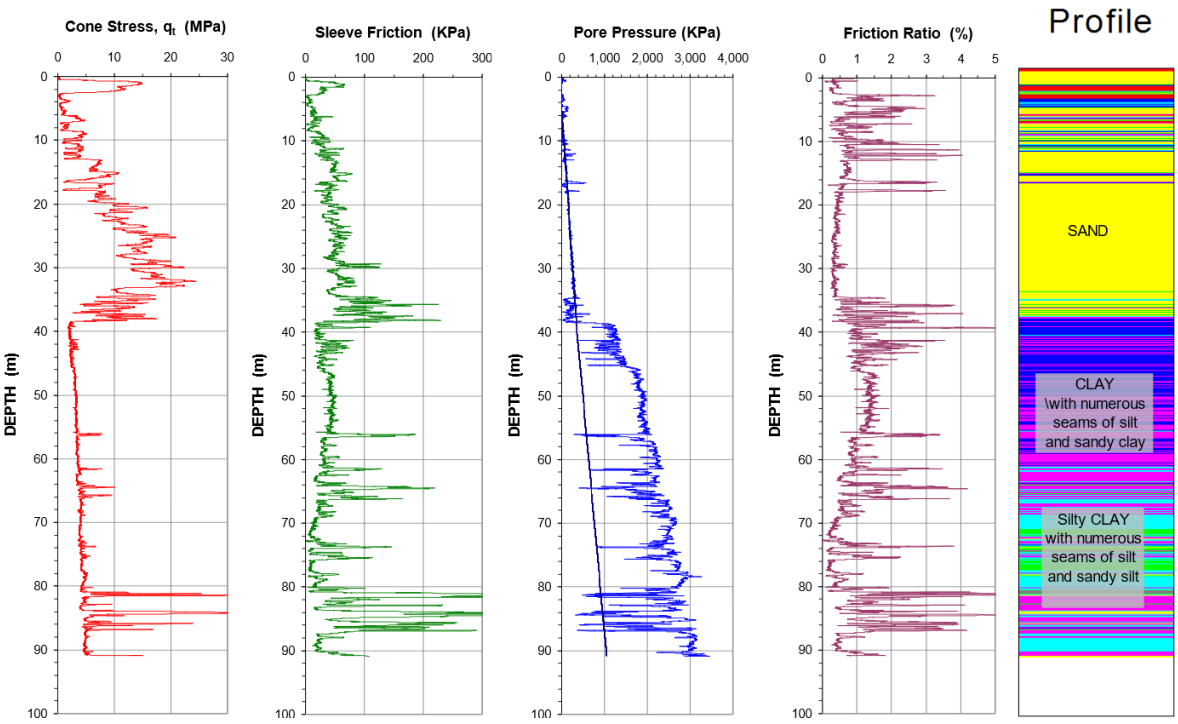

Figure 19. Soil profile obtained from CPTu data (Fellenius 2018, p. 2-19).

SCPTu (Seismic Piezocone Penetration Test) includes a geophone inside the penetrometer, which is used to measure the arrival times of shear waves generated on the ground surface close to the cone rod. The shear wave is generated by horizontally striking a steel plate placed on the surface and the time between the strike and the arrival of the wave to the geophone is recorded. Impacts are given at intermittent depths and the travel time difference between the

geophone at the previous depth and current depth is evaluated. The result gives the shear wave velocity for the soil between the two depths. (Fellenius 2018, p. 2-25)

Numerous methods for profiling soils using CPT data have been developed in past decades. Begemann (1965) can be considered a pioneer in the field, having discovered that soil type is not strictly dependent on cone resistance or sleeve friction, but rather the combination of them. According to Begemann's research, soil type can be determined from the ratio of sleeve friction and cone resistance, known as friction ratio R_c. The data was only gathered from a single site and can only be applied directly there, however the data is important at a general qualitative level. Begemann's soil profiling chart is shown in Figure 20 and friction ratios of soil types in Table 1. The friction ratios are indicated by the slopes of the lines. (Fellenius & Eslami 2000, pp. 2–3)

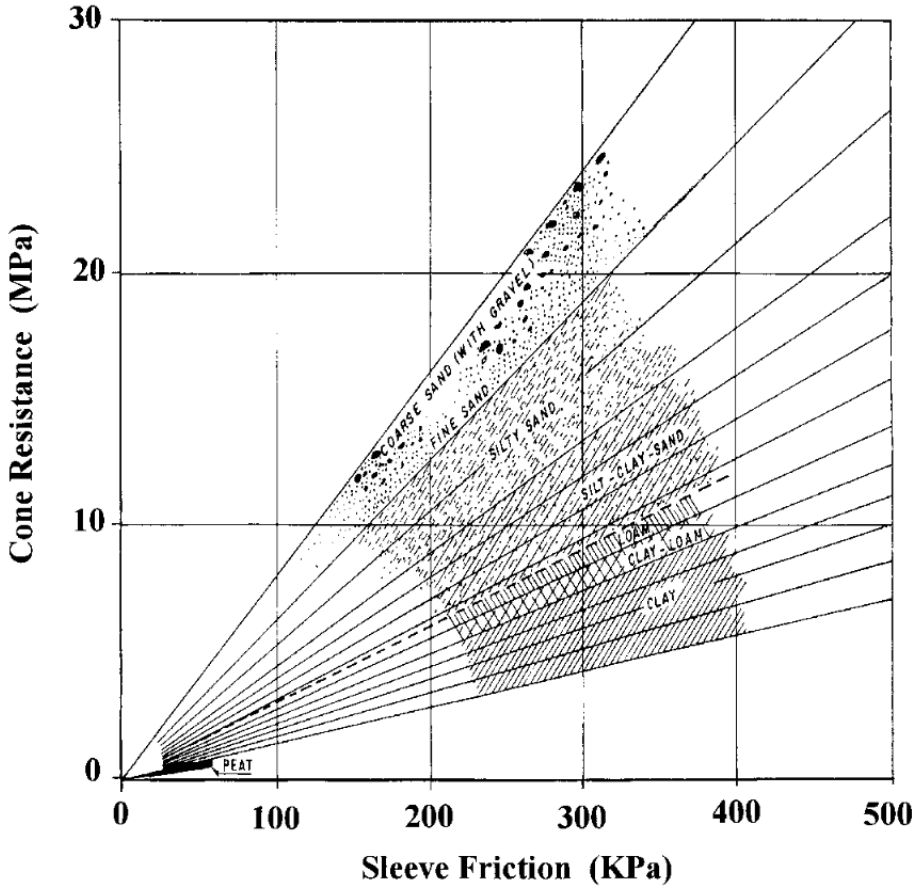

Figure 20. Begemann's soil profiling chart (Fellenius & Eslami 2000, p. 2).

Table 1. Soil types by friction ratio according to Begemann (1965) (Fellenius & Eslami 2000, p. 3).

Soil type	**Friction ratio (%)**
Coarse sand with gravel through fine sand	1.2 – 1.6
Silty sand	1.6 – 2.2
Silty sandy clayey soils	2.2 – 3.2
Clay and loam, and loam soils	3.2 – 4.1
Clay	4.1 – 7.0
Peat	>7.0

An improved chart incorporating the data from Begemann was proposed by Schmertmann (1978), presented in Figure 21. The chart includes boundaries for dense and loose sand and also consistency of clays and silts. These boundaries are not interpreted from the CPT results, but are instead imposed by definition. The downside of the Schmertmann method is that the chart is presented as a plot of cone resistance and friction ratio. As friction ratio is obtained from cone resistance, this results in cone resistance being plotted against its inverse value, causing distortion in the data. For example, the accuracy of friction ratio values decreases with low values of cone resistance. (Fellenius & Eslami 2000, p. 3–5)

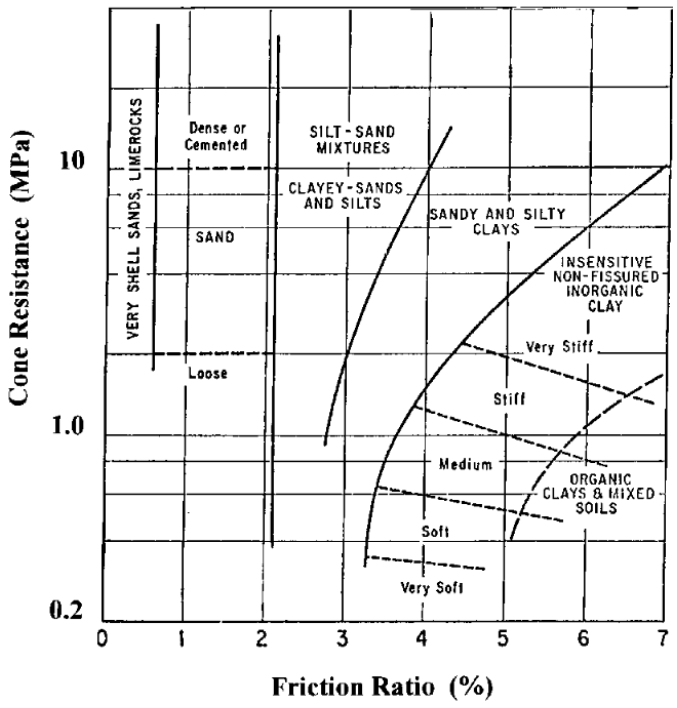

Figure 21. Schmertmann's soil profiling chart (Fellenius & Eslami 2000, p. 4).

The first soil profiling chart based on electric cone penetrometer data was proposed by Douglas & Olsen (1981), shown in Figure 22. In addition to soil type zones, the chart includes trend curves for liquidity index, earth pressure coefficient, fines content, grain size and void ratio. The chart is similar to the Schmertmann chart in Figure 21, however there is a difference in soil type response. This can be seen from the soil type envelope curves, which curve upward on the Douglas & Olsen chart and downward on the Schmertmann chart. (Fellenius & Eslami 2000, p. 5)

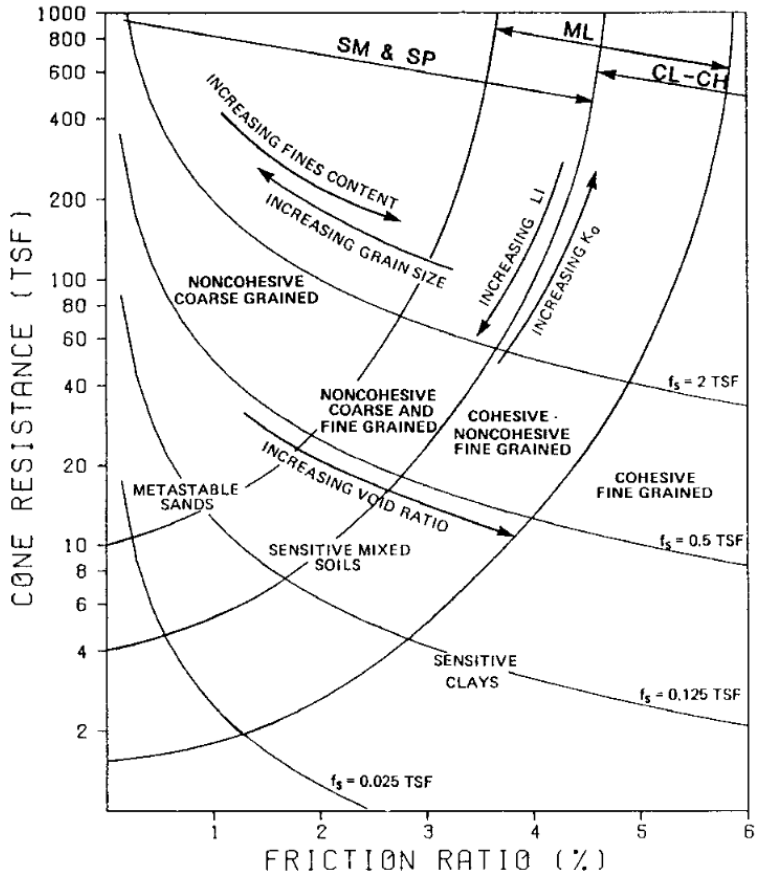

Figure 22. Douglas & Olsen soil profiling chart (Fellenius & Eslami 2000, p. 5).

Soil profiling charts based on CPTu data were presented by Robertson et al. (1986). In this method, soils can be profiled according to cone resistance corrected for pore pressure at the cone shoulder q_t and pore pressure ratio B_q, described by equations (Robertson et al. 1986, pp. 1263–1265):

$$q_t = q_c + u_2(1 - a_c) \tag{66}$$

$$B_{\mathrm{q}} = \frac{\Delta u}{q_{\mathrm{t}} - \sigma_{\mathrm{v0}}} \tag{67}$$

where a_{c} is the net area ratio, Δu is the excess pore pressure and σ_{v0} is the total overburden stress.

As seen in Figure 23, the charts are divided into 12 zones according to soil type. The zones are (Robertson et al. 1986, p. 1267):

1. Sensitive fine-grained
2. Organic material
3. Clay
4. Silty clay to clay
5. Clayey silt to silty clay
6. Sandy silt to clayey silt
7. Silty sand to sandy silt
8. Sand to silty sand
9. Sand
10. Sand to gravelly sand
11. Very stiff fine-grained (overconsolidated or cemented)
12. Sand to clayey sand (overconsolidated or cemented)

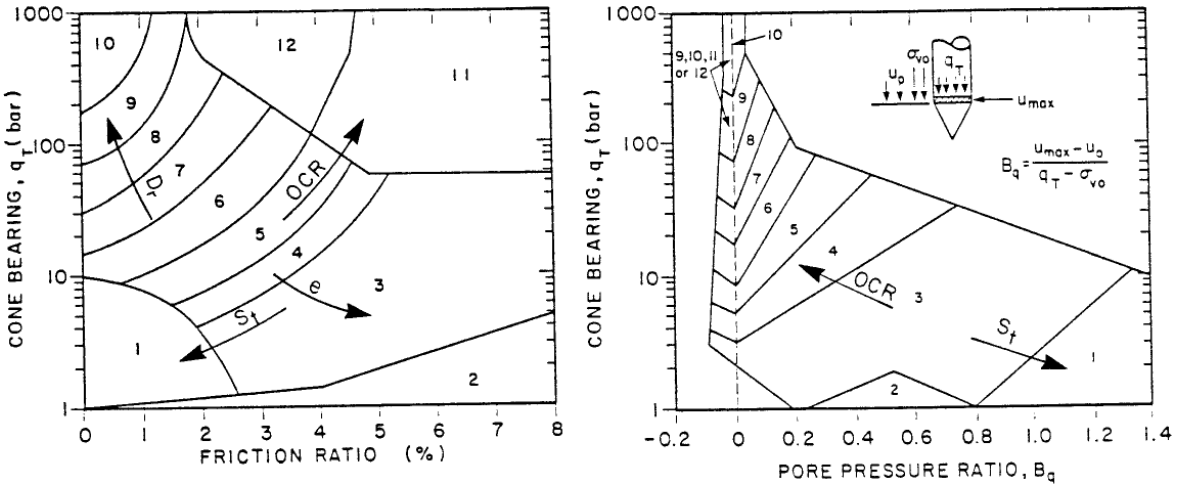

Figure 23. Soil profiles based on corrected cone pressure and pore pressure ratio (Robertson et al. 1986, p. 1267).

An improvement to the chart above was later proposed by Robertson (1990), which includes normalized cone resistance q_{cnrm} and normalized friction ratio R_{cnorm}, obtained from equations (Robertson 1990, p. 153):

$$q_{\mathrm{cnrm}} = \frac{q_{\mathrm{t}} - \sigma_{\mathrm{v0}}}{\sigma'_{\mathrm{v0}}} \tag{68}$$

$$R_{\mathrm{cnrm}} = \frac{f_{\mathrm{s}}}{q_{\mathrm{t}} - \sigma_{\mathrm{v0}}} \times 100\% \tag{69}$$

The charts, presented in Figure 24, are mostly similar to the previous ones, but the number of zones has been reduced to 9. They are (Robertson 1990, p. 153):

1. Sensitive, fine-grained
2. Organic soils – peats
3. Clays – clay to silty clay
4. Silt mixtures – clayey silt to silty clay
5. Sand mixtures – silty sand to sandy silt
6. Sands – clean sand to silty sand
7. Gravelly sand to sand
8. Very stiff sand to clayey sand (heavily overconsolidated or cemented)
9. Very stiff, fine-grained (heavily overconsolidated or cemented)

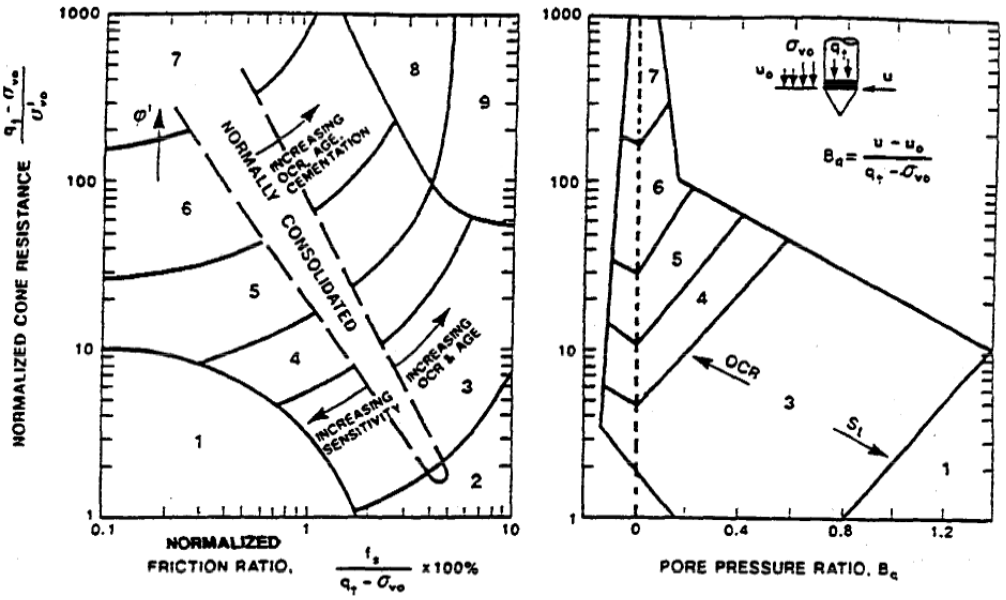

Figure 24. Soil profiles based on normalized cone resistance and normalized friction ratio (Robertson 1990, p. 153).

CPT data can be used to calculate some of the soil parameters required in the models presented above, namely φ and γ_s. The internal angle of friction φ can be assumed to be equal to the peak angle of friction ϕ', which can be assessed using multiple different methods. Using only cone resistance from CPT or normalized cone resistance and pore pressure ratio from CPTu data, ϕ' can be expressed as (Robertson & Cabal 2012, pp. 45–47):

$$\phi' = 17.6° + 11 \log q_{\mathrm{cnrm}} \tag{70}$$

$$\phi' = 29.5° \cdot B_{\mathrm{q}}^{0.121}\left[0.256 + 0.336 B_{\mathrm{q}} + \log q_{\mathrm{t}}\right] \tag{71}$$

Soil unit weight can be calculated from (Robertson & Cabal 2012, p. 35):

$$\frac{\gamma_{\mathrm{s}}}{\gamma_{\mathrm{w}}} = 0.27 \log R_{\mathrm{c}} + 0.36 \log \frac{q_{\mathrm{t}}}{p_{\mathrm{a}}} + 1.236 \tag{72}$$

where p_a is atmospheric pressure. By substituting Equation 72 to Equation 64, soil density ρ can be obtained.

According to Aksoy et al. (2016, p. 315), skin friction angle δ is commonly assumed to be equal to 2/3 of the internal friction angle φ in engineering applications. A more detailed chart for determining δ for different materials developed by Aksoy et al. is shown in Figure 25.

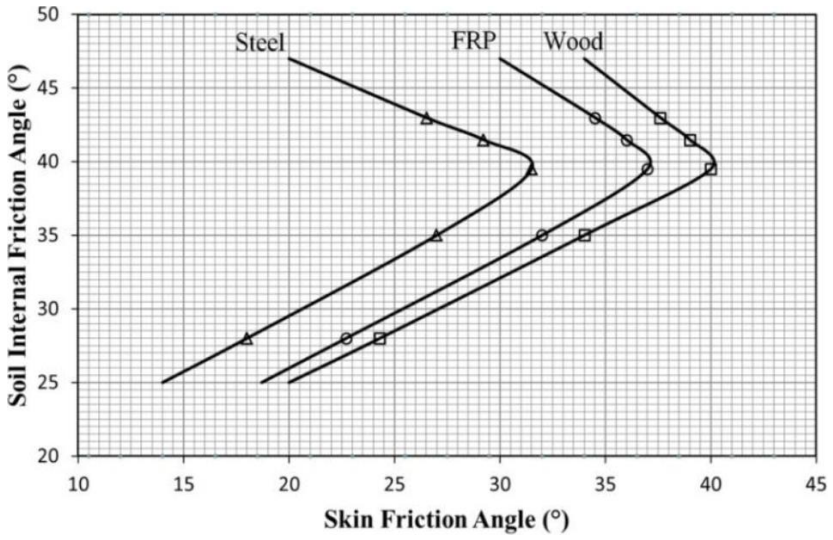

Figure 25. Skin friction chart (Aksoy et al. 2016, p. 321).

The coefficients of friction μ and μ_1 are related to the angles of friction according to equations (Zhang & Ding 2016, p. 191):

$$\mu = \tan(\varphi) \tag{73}$$

$$\mu_1 = \tan(\delta) \tag{74}$$

No soil testing will be carried out in this thesis and all soil data required for the simulation will be obtained from outside sources.

2.6 Simulation software

Mevea is real-time simulation software for simulating working machines based on multibody dynamics. The software uses its own physics engine, which allows accurate simulation of mechanics, hydraulics, power transmission and the operating environment of the machine. The software consists of three main modules: Mevea Modeller, Mevea Solver and Mevea I/O Toolbox. Mevea Modeller is used for creating and editing virtual machine models, including the hydraulics and power transmission, and the environment. Mevea Solver runs the model and records the results for reviewing and research. Mevea I/O Toolbox can be used to connect external systems to the simulation. These include for example control systems and co-simulation software. (Mevea 2020b)

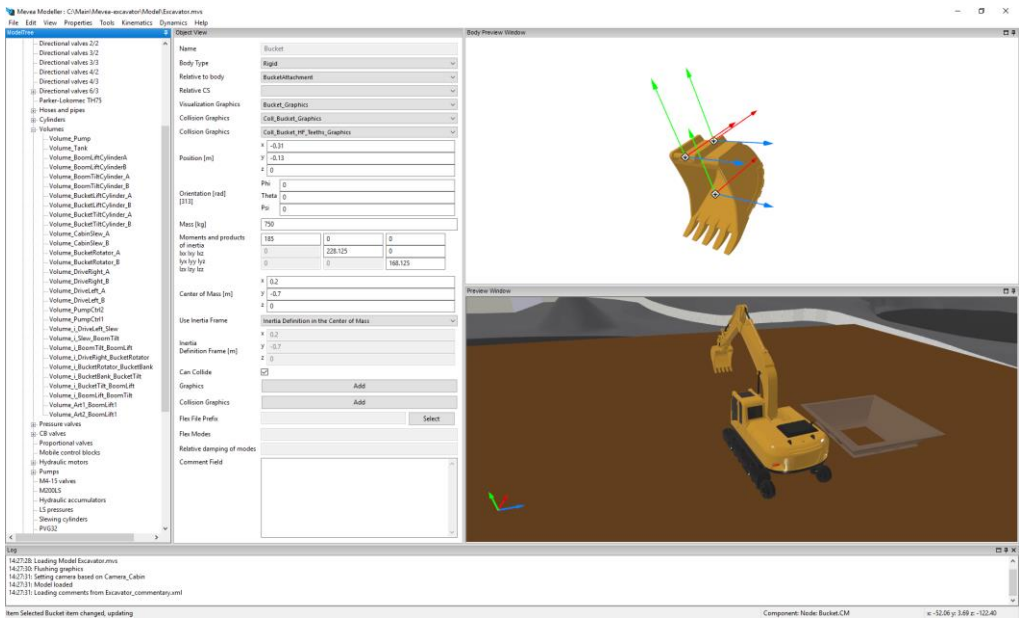

Figure 26. Mevea Modeller user interface (Mevea 2021).

As Mevea does not currently have functionality for multilayered soils, the auger and soil mechanics must be modelled with other software utilizing co-simulation. The software inspected for auger and soil modelling are Xcos and Simulink.

Xcos is a graphical editor for modelling dynamic systems, which is part of an open source computational software called Scilab. Scilab includes a large variety of mathematical functions and functionalities, such as simulation, 2D and 3D visualization and signal processing. According to Scilab, Xcos is typically used for mechanical systems, hydraulics and control systems. (Scilab 2020)

Simulink is a graphical programming environment based on Matlab developed by MathWorks. While it is typically used for simulating dynamic systems, Simulink can be used for a large variety of different applications such as computer vision or artificial intelligence with the several types of toolboxes offered for it. C/C++ code can also be generated from Simulink models. (MathWorks 2020)

Mevea has provided the interfaces required for coupling Xcos and Simulink with their software. The software versions used are Scilab 6.0.1 and Matlab R2020a. Which software the models are made with will be determined based on performance tests with a piling simulation model.

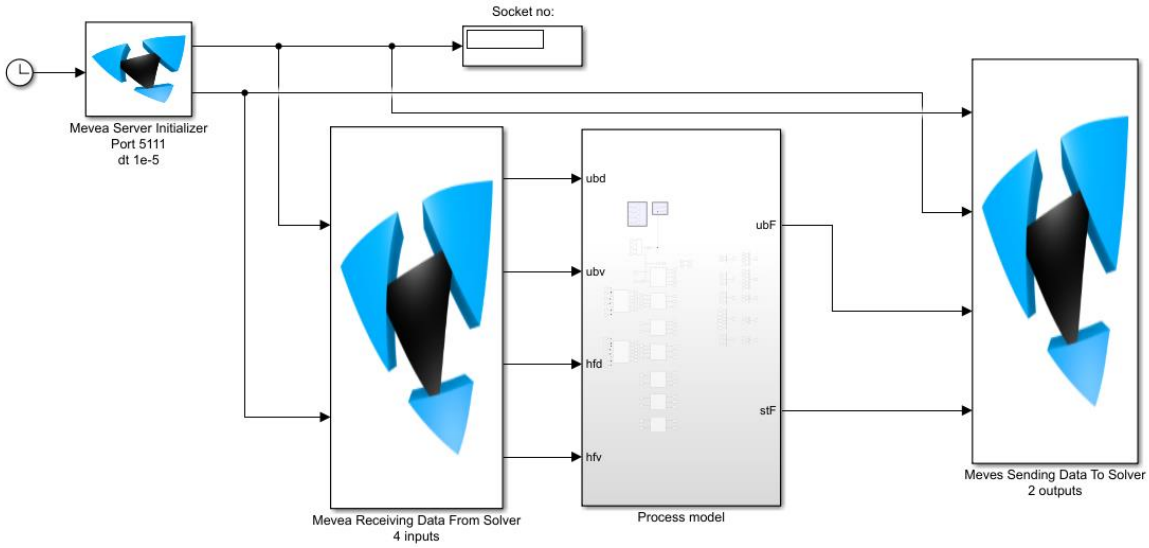

Figure 27. Piling process model in Simulink with Mevea interface.

3 RESULTS

The performance test between Xcos and Simulink was used to select the software for building the drilling process model. The process models were made based on the methods shown in the previous chapter, with some modifications. The following chapter will also describe the general soil profile of the test drilling site. Finally, comparison between simulation results and measurements will be presented.

3.1 Software comparison

Performance comparison between Xcos and Simulink was done using an existing pile driving simulation model, which consists of a simplified Mevea model with only the hydraulic impact hammer connected to the leader. The model uses a piling process model made with Xcos to simulate the piling forces. The existing model was converted into a Simulink model and tested with manual inputs to confirm that it produces the exact same results as the Xcos model. Interfacing with the Mevea model proved more problematic, as the Xcos model used an ode4 solver which caused issues with the Simulink model. Using the ode4 solver in Simulink caused Mevea to freeze during the initial time step, and despite numerous attempts this problem could not be solved. The solver was changed to ode2 as a result.

To compare the simulation performance of the software, the loop duration was recorded in Mevea. The goal was for loop duration to be under 0.9 ms, which is the time step used in the Mevea model. During the simulation, intermittent hammer impacts were also done with the impact hammer in Mevea to see how it affects simulation speed. In addition to normal mode, the Simulink model was also run in rapid accelerator mode. This mode generates an executable of the Simulink model, greatly improving simulation time. The results are presented in Figure 28.

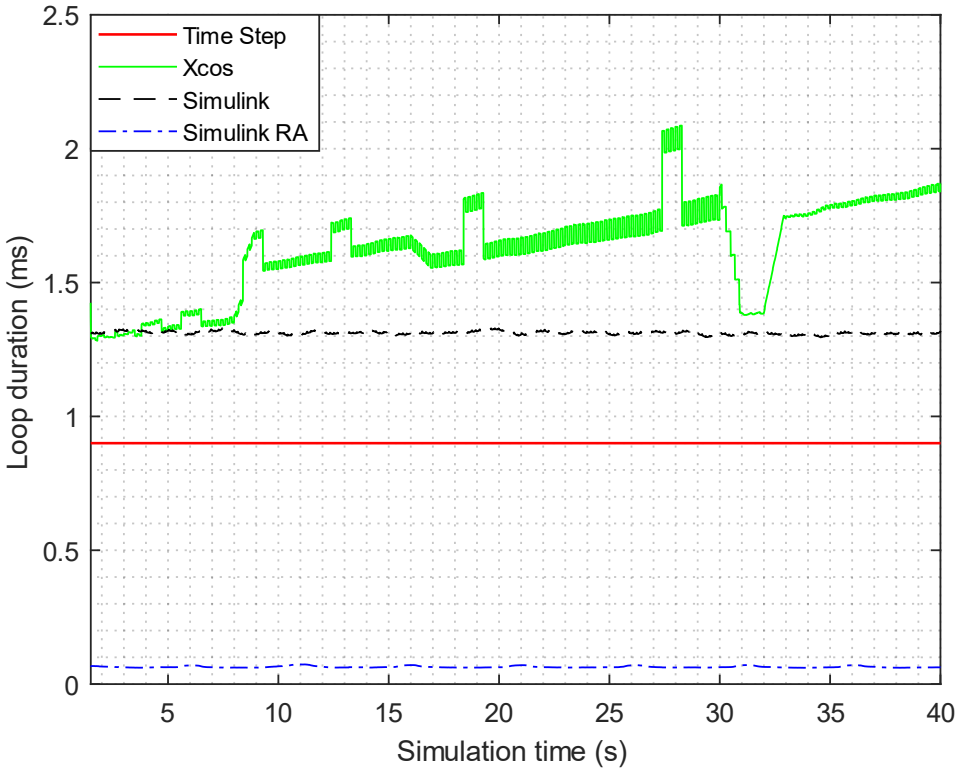

Figure 28. Simulation speed comparison between Xcos and Simulink.

Xcos was found to be very unstable. It was prone to crashing and got slower with time as can be seen from the graph. The exact cause of this is unknown, but one possible reason is some sort of memory leak. Hammer impacts can be seen as noticeable spikes, which also increase in size along with simulation time. It was also too slow, going slightly under 1.3 ms at its fastest.

Simulink was noticeably more stable. Although it did not meet the speed requirement in normal mode either, the loop duration is consistently around 1.3 ms and the model stayed stable during longer simulations as well. The impacts can be seen as slight bumps. When run in rapid accelerator mode however, the simulation is significantly faster. The loop duration is consistently under 0.1 ms and just like in normal mode the impacts slow the simulation down only slightly. The Simulink model did not crash in either mode.

Due to these test results, the drilling process and soil models were chosen to be made with Simulink.

3.2 Test drilling site

Test drilling was done in Suonenjoki, Finland. Detailed information on the soil at the test site was not available, however a rough understanding could be obtained from a geological survey done at the site in 1980. The survey was done utilizing the WST (Weight Sounding Test) soil profiling method in various boreholes around the site. It was concluded that in general the top layer consists of coarse silt up to a depth of 2 meters, followed by layers of fine sand ranging from medium stiff to stiff. Stiffness of the silt layer was not mentioned, but from the WST graphs available for some of the boreholes it was determined to be stiff. The maximum borehole depth in the survey was 14.5 meters and deeper holes were deemed unnecessary as the soil types did not noticeably change. Ground water level was reported to be at the depth of 1.5 meters. Parameters for these soil types are presented in Table 2 below.

Table 2. Properties of coarse silt, fine sand and sand (Liikennevirasto 2012, Appendix 1).

Soil type		Volumetric weight (kN/m^3)		Internal angle of friction (°)	Penetration resistance	
		Above ground water level	Below ground water level		CPT q_c (MPa)	WST *Pk*/0.2 m
Coarse silt	Soft	14 … 16	9 …	28	< 7	< 40
	Medium stiff			30	7 … 15	40 … 100
	Stiff	16 … 18	11	32	> 15	> 100
Fine sand	Soft	15 … 17	9 …	30	< 10	20 … 50
	Medium stiff			33	10 … 20	50 … 100
	Stiff	16 … 18	11	36	> 20	> 100
Sand	Soft	16 … 18	10 …	32	< 6	10 … 30
	Medium stiff			35	6 … 14	30 … 60
	Stiff	18 … 20	12	38	> 14	> 60

In the report it was also noted that the soil in the area is not consistent and there can be significant local variation between boreholes. The soil contains sewage sludge in some locations while some spots are very rocky. This was confirmed during the test drilling, as it was reported that at some locations the soil is so soft that the auger sinks with only its own

weight and at some locations the soil is very stiff. Thus, no single universal soil profile could be made for all the boreholes drilled during the testing. Soil profiles were instead approximated for each borehole individually.

The above soil types and parameters could only be used for the FDP model, as reports from the CFA test drilling indicated that the soil there consisted mainly of peat, which was not mentioned at all in the survey data. And since no soil testing could be done, approximate values for peat had to be used. The entire sub-layer was assumed to consist of normally consolidated peat, with a reported slightly tougher frozen layer at the surface. According to Carlsten (1988) typical values of φ for normally consolidated peat range from 27.1° to 32.5° and c is typically 2.4 kPa, as shown in Figure 29. Adhesion c_a is assumed to be equal to c.

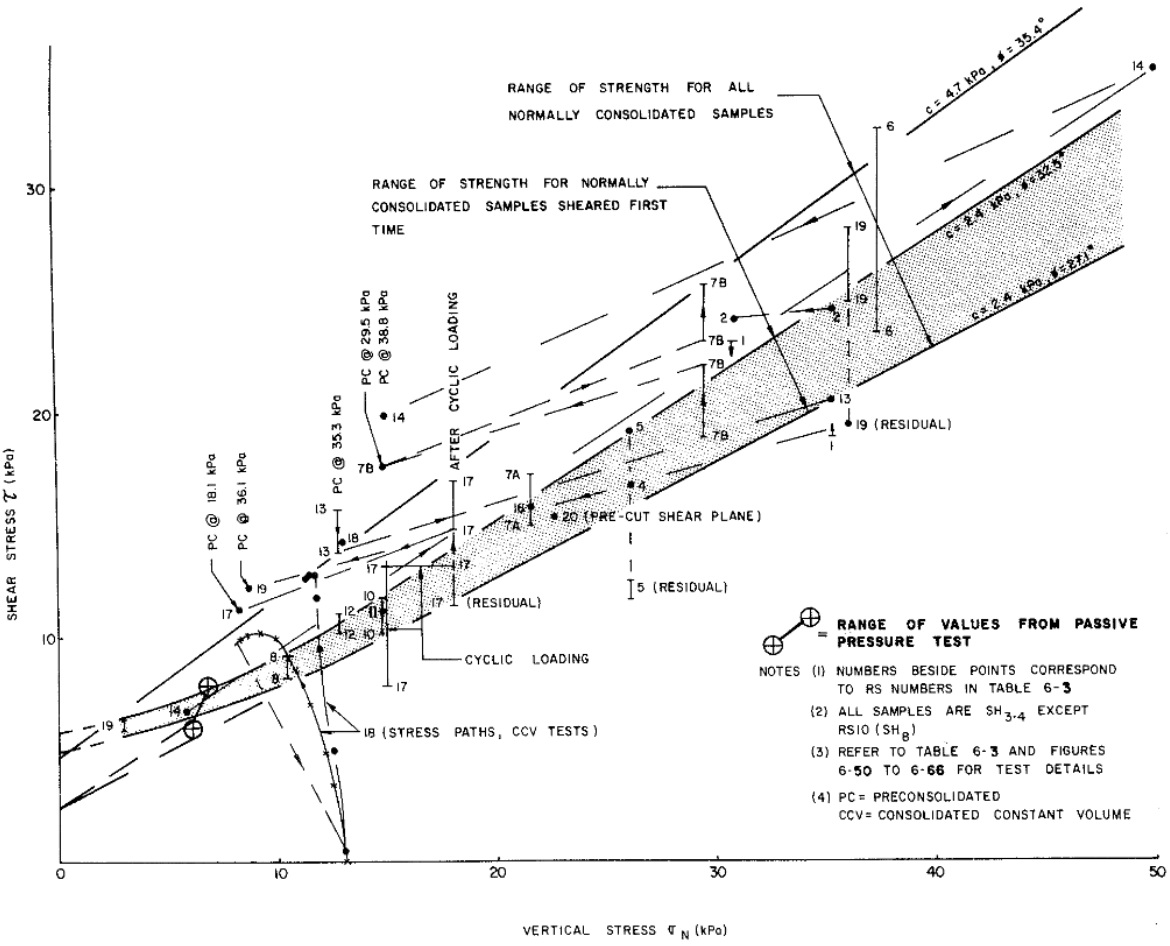

Figure 29. Shear test results for peat (Carlsten 1988, p. 15).

3.3 Soil model

The developed soil model consists of two parts. The first part is used for switching layers and selecting the soil properties for the current layer. The block takes the soil properties, soil layer depths and penetration depth as inputs and outputs the corresponding values at the current depth. During testing it was noticed that the layer switching was initially too abrupt. The immediate switching from one value to another caused noticeable and sudden jumps in the simulated drilling loads. To counter this, a functionality was added to smoothen the transition between different layer values.

The second part is used for storing values from the previous layers. This block has a very simple functionality in the FDP model, as it is mainly used to store the value of overburden stress in the previous layers, which is independent of the penetration and rotational velocity of the auger. The CFA model however has a more prominent and complex use of this block. The CFA model assumes that the soil affects the auger along its whole length, meaning that the motion of the auger still affects the values in the previous layers. Because of this, the load caused by each of the previous layers must be constantly recalculated.

Parametrization is achieved by using a Matlab M-file to input the soil data into Simulink. The user inputs the soil property and layer depth values into corresponding arrays in the file, which is run before the simulation is started to upload the values into Matlab workspace. These values are then read by Simulink during the simulation. Any number of soil layers can be inputted by the user. The same file also contains variables for inputting the auger dimensions.

3.4 Continuous flight augering process model

Initial testing revealed some problems with the model. There were large spikes several magnitudes higher than normal observed in the simulated cutter forces. The main cause for this was identified to be the side crescent failure mode of the cutters. For this reason, force V_2 was ignored from the calculation of V_b. Angle γ would sometimes obtain complex values, which was determined to be caused by the variable d. This was fixed by replacing d with critical depth d_c according to Godwin & Spoor's (1977) original equation. In this case d_c was assumed to be the vertical distance between the cutter's tip and midpoint. The simulated torque increased too rapidly as a function of depth, so T_a was divided by z. Finally, some

correction factors had to be applied to the calculation of F and T so the results would be in the proper range. Thus, equations 39, 51, 54 and 55 were changed to:

$$\gamma = \cos^{-1}\left(\frac{\sin(\beta_1)\cos(\alpha_1)}{d_c \sin(\alpha_1+\beta_1)}\right) \tag{75}$$

$$V_b = -P_1 \cos(\alpha_1 + \delta) + c_a w d \sin(\alpha_1) \tag{76}$$

$$F = \frac{F_a + 1.1F_b}{5.5} \tag{77}$$

$$T = \frac{0.1T_a}{z} + 2T_b \tag{78}$$

The process model uses v, n and z as inputs from Mevea. Validation of the model was done without interfacing it with Mevea. Instead, the penetration rate, rotational speed and penetration depth measured during the drilling process were inputted into the model and the obtained torque and force were compared with the measurement data. The test drilling was done with a 6 meter long single-helix auger with two cutters at the tip. Test results for the CFA model are presented in Appendix I.

3.5 Full displacement piling process model

While initial testing showed good results, some changed had to be made to the FDP model as well. During the initial insertion of the auger into a soil layer, the torque and thrust values tended to lag at a low value and sharply increase after the whole tip had been inserted into the soil. which was very unnatural behavior when compared to the measurement data. Coefficients η_1, η_2 and η_4 were identified as possible causes and this behavior was corrected by using the inverse values of these coefficients. The simulated torque was observed to be roughly ten times higher than the measured torque, so M_T is multiplied by a correction factor of 0.1.

Finally, the simulated values for thrust Q_{TV} did not match the measured values. However, it was found that, as was theorized in equation 65, thrust did indeed seem to be related to torque. When the auger is rotating during penetration, Q_{TV} was observed to be proportional

to the value of total torque M_T instead of only shaft torque. Based on these observations, Q_{TV} was calculated as:

$$Q_{TV} = \frac{M_T}{40} \tag{79}$$

This only applies during rotation, so a different method will have to be developed to determine thrust when penetrating the soil without rotating the auger. It is also unclear if these large initial inaccuracies were a consequence of the shape of the auger tip, which is different from the one shown in chapter 2.4. The auger tip used in the test drilling is shown in Figure 30.

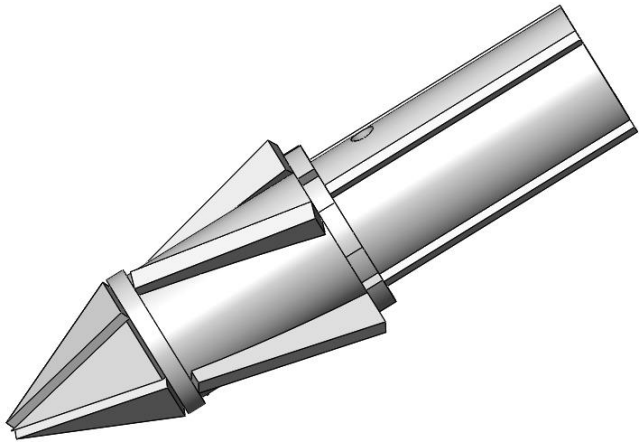

Figure 30. FDP auger tip used in the test drilling.

Comparison to measurement data was done similarly to the CFA model with the same inputs and outputs. Test results for the FDP model are presented in Appendix II.

3.6 Mevea model

The Mevea model is a simplified version of the MPx90 machine, consisting only of parts that are required for the drilling operation. The mechanical parts can be divided into two categories: telescope leader and rotary head.

The telescope leader consists of seven rigid bodies connected to each other by fixed joints. The bottom of the leader is fixed to the ground. The rotary head consists of a single rigid body connected to the middle leader by a translational joint. The rotary head also houses

pulleys for the ropes. A work tube is connected to the rotary head by a rotational joint and an auger tip is fixed to the work tube. Hydraulic motors in the rotary head are connected to a body-to-body force between the rotary head and work tube, which is used for rotating the auger. External soil resistance forces are included as single body forces at the auger tip. Graphics of the bodies were converted to .stl files from SolidWorks models. Mass and inertia values for the bodies were also obtained from SolidWorks. Currently the model only has graphics for an FDP auger, but a CFA auger can still be modelled by inputting its mass and inertia values into the work tube and the values of a drill bit into the auger tip. Model topology is presented in Figure 31 and a picture of the model is shown in Appendix III.

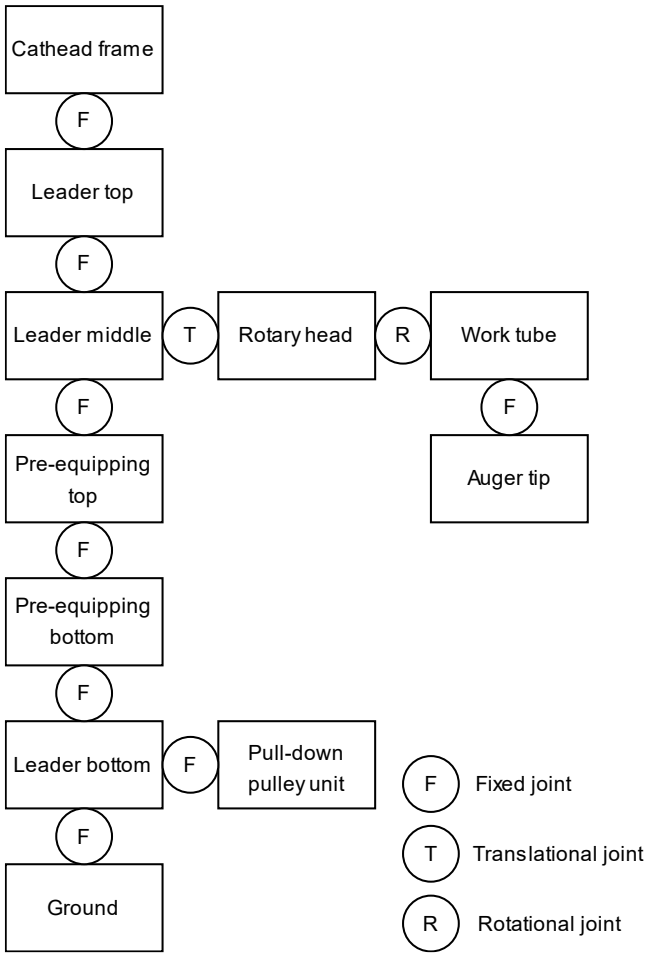

Figure 31. Model topology.

The rotary head is moved up with a pull-up rope and down with a pull-down rope. The ropes are connected to winches via systems of pulleys. The cathead frame houses pulleys for both ropes, while the pull-down pulley unit houses pulleys only for the pull-down rope. Pulleys

are also attached to the middle leader and rotary head. The winches and the end of the pull-up rope are attached to ground, while the end of the pull-down rope is attached to the rotary head.

To simplify the model development, most of the hydraulics except for the rotary head were copied from an existing PMx27 simulation model. The most important components, such as pumps, hydraulic motors, and valves, were changed to the ones used in MPx90 machines. The time step of the model is set to 0.9 ms.

The model is connected to Simulink via a socket interface. As the model was found to be prone to freezing at the initial time step when there were too many inputs and outputs, their number had to be limited. Currently the model outputs drilling depth, penetration rate and rotational speed while taking soil resistance force and torque as inputs, as shown in Figure 32.

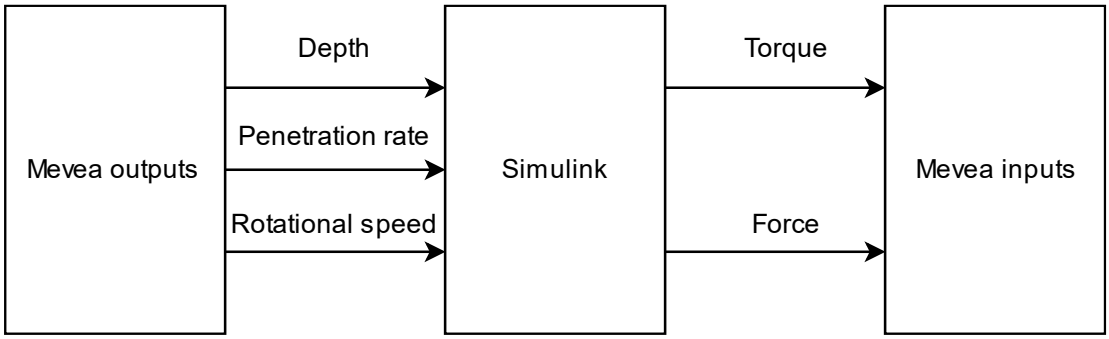

Figure 32. Co-simulation I/O flowchart.

The FDP model has no connection issues with the Mevea model with any solver or time step settings. The CFA model however was more problematic. It was found out that the interface works correctly only when using the ode4 Runge-Kutta solver with a time step of 0.01 ms. Any other settings either cause the simulation to freeze at the initial time step or crash. Simulation speed when interfaced with the Simulink models is presented in Figure 33. Both process models use an ode4 solver and a 0.01 ms time step.

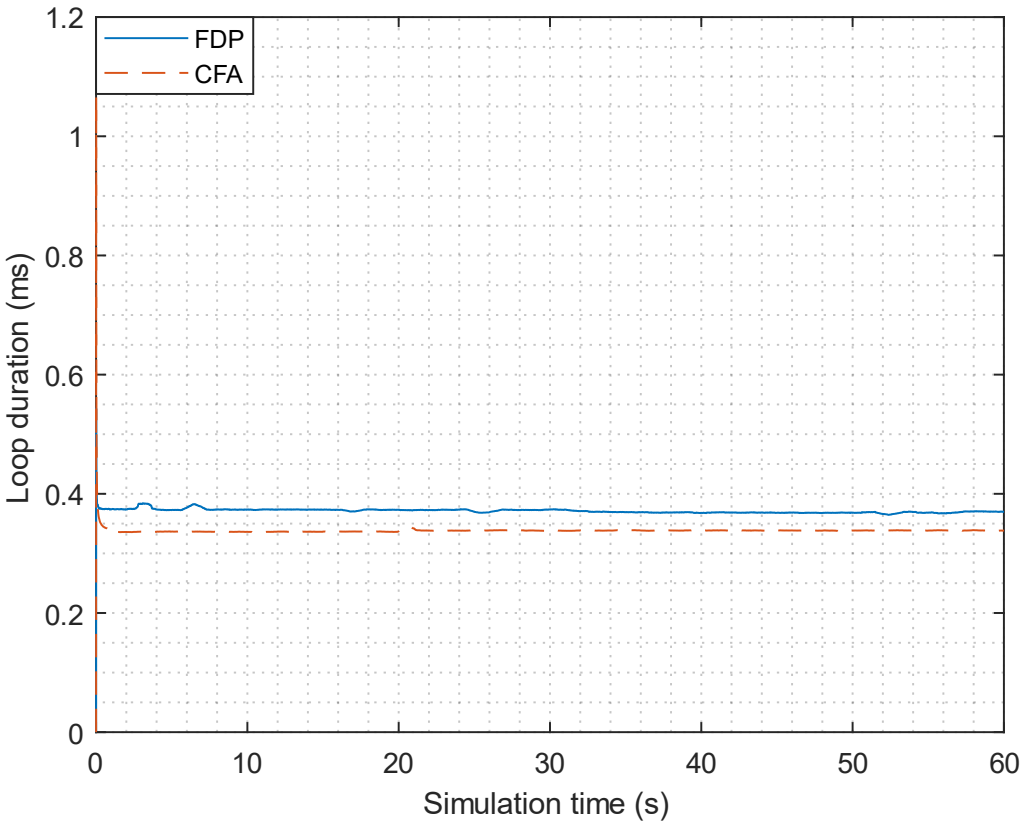

Figure 33. Simulation speed of the process models.

4 ANALYSIS

Both process models were determined to give sufficiently accurate results. Interestingly, both models calculated torque more accurately than force. The difference in force between the processes was unexpected though.

According to theory, force and torque during the CFA process are produced by components of the same forces acting in different directions. This should result in a clear relation between them, which can be seen from the simulation results. The measurements from test drilling showed otherwise. No discernible relation can easily be seen from the obtained results. As it is unknown which factors other than the ones presented here contribute to generating force during CFA drilling, developing another method will be challenging. The error seems to get smaller as depth increases. The results show that starting from a depth of around 3 meters, the simulated values are generally close to the measured values.

Conversely, results from FDP drilling showed a distinct relation between torque and force just as theory suggested. Force during the FDP process can be said to generally be a multiple of torque, though it is apparent that there are also some other factors influencing it. The main issue encountered during this project was that torque is zero when the auger is not rotating, which also results in force being zero. However as can be assumed and verified from the measurement data, a resistance force still exists when pushing the auger into the ground without rotation. Some attempts were made to calculate this force using cone resistance, but no successful way that would work for each borehole was yet found.

Although the biggest differences were between simulated and measured force, torque calculations also need improvement. Despite the simulated values generally following the measured values well, the error is very large at times. It is also noteworthy that the measured and simulated values of the CFA model appear to be mirrored. An example of this in borehole 1 is shown in Figure 34. From the figure it can be seen that the simulated value increases as the measured value decreases and vice versa. This behavior can be observed in all boreholes. The most probable cause for this is one or more of the forces in the model having a wrong direction.

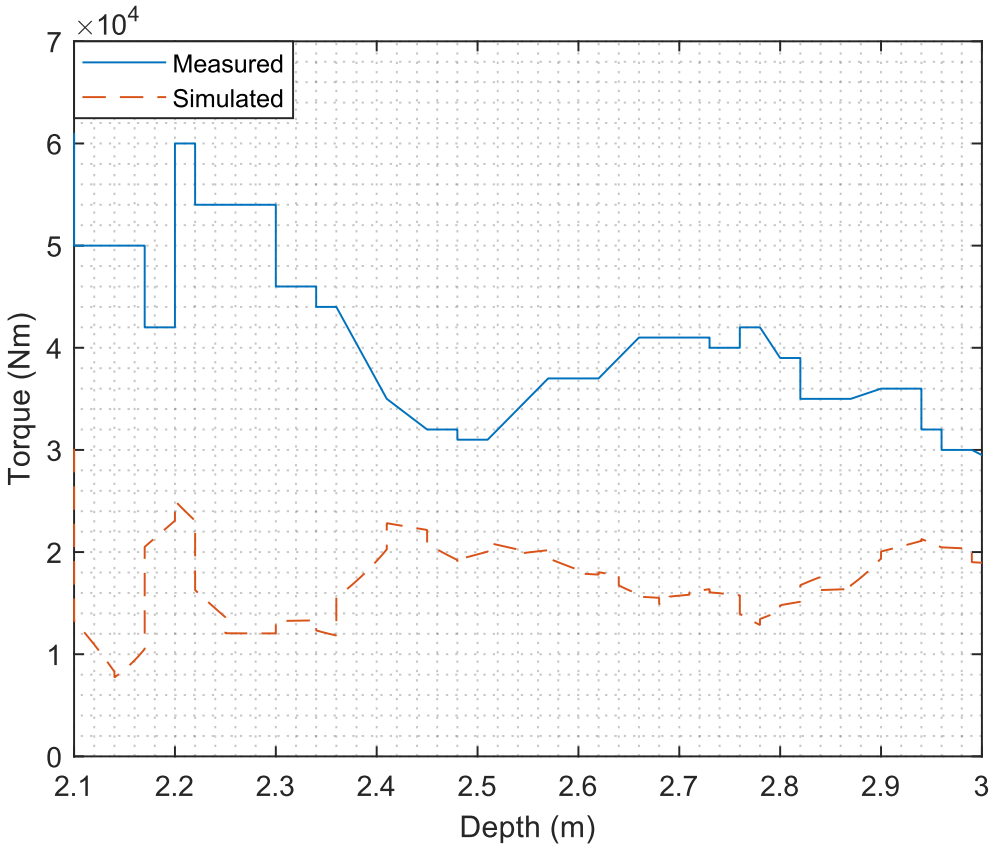

Figure 34. Difference between measured and simulated torque in CFA borehole 1.

All the simulated FDP values have a clear peak around the 2 m mark. Clear causes for this are the shape coefficients, suggesting that they still require some tuning. FDP results also stop being accurate at a depth of roughly 8 m. This can most clearly be seen in boreholes 2 and 3. The most likely cause for this was identified to be t_{Tb}, which starts increasing more rapidly from 8 meters onwards. An example of this in borehole 2 is shown in Figure 35. Because of this the simulated torque remains at over 200 kNm and keeps increasing instead of decreasing to around 80 kNm like the measured torque. Further inspection and tuning of the base friction is required to produce better results.

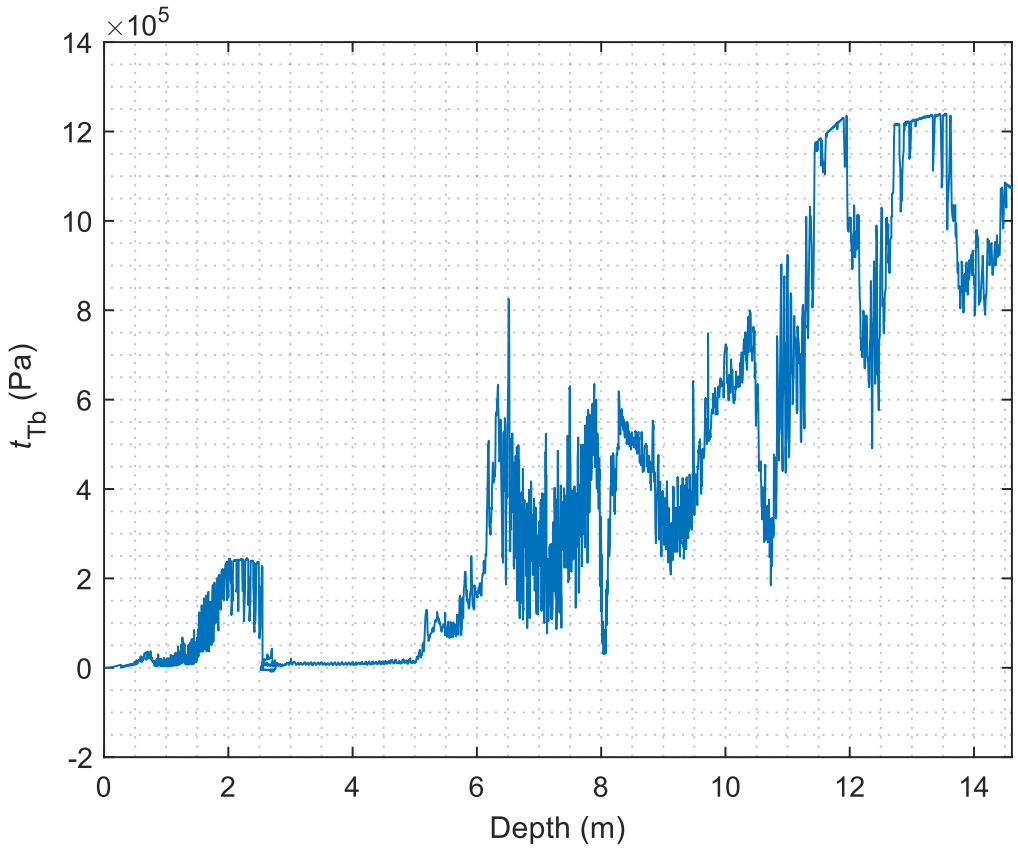

Figure 35. Simulated t_{Tb} in FDP borehole 2.

It should also be noted that the measured force used to pull the rotary head down, known as pull-down force, is not an actual measured value. The pull-down force recorded during the drilling is a calculated value obtained from the measured pull-up force. Due to this, the results for forces may not be reliable.

The lack of detailed soil data at the testing site was a large hindrance to this project. Although some data was available, assumptions still had to be made. It is possible that the inaccuracies in the models are caused by false assumptions in layer depths, soil types and their corresponding values. On the other hand, it is also possible that even the best results obtained from the simulations may just be caused by conveniently selected values, which might not reflect the actual soil properties in these boreholes. More testing with detailed soil data will have to be conducted in the future to gain a better understanding of the accuracy of these models and possibly be used to develop better ones. It would also reveal whether or not the changes made in the equations are specific to this site.

Simulation speed when interfaced with both process models fulfills the set requirement of being under 0.9 ms. Both models achieve a loop duration of under 0.4 ms with the CFA model being slightly faster. There are no noticeable spikes except for slight bumps at the beginning of FDP simulation, which are most likely caused by the ropes tightening. The ropes are notable for being very computationally heavy. The speed remains constant during the simulation and does not slow down with time.

The research goals set for this project were successfully reached. The presented analytical models based on the friction between the auger and soil were found to provide sufficiently realistic results when compared to a physical system. To calculate the loading, the models use the motion of the auger which is in turn modelled in Mevea. By modelling the drilling process with Simulink using the rapid accelerator simulation mode, real-time simulation is achieved. As for parametrization, it could be achieved with Simulink by running an M-file to upload the parameters into Matlab workspace, which Simulink then accesses. List of the required soil and auger parameters are presented in Table 3 and Table 4. The developed soil model was also copied into the existing pile driving model and verified to work.

Table 3. FDP process model user inputted parameters.

Soil	Layer depths
	n_p
	q_{cb}
	q_{cs}
	γ_s
	ρ
Auger	D_s
	D_{s0}
	h_{s1}
	h_{s2}
	h_{s3}
	h_{s4}
	n_c
	s

Table 4. CFA process model user inputted parameters.

Soil	Layer depths
	c
	c_a
	γ_s
	δ
	ρ
	φ
Auger	l
	s
	r
	r_1
	r_2
	r_3
	r_4
	r_5
	r_6
	w
	α
	α_1
	n_c

The FDP model requires six soil parameters and eight auger parameters, while the CFA model requires seven soil parameters and 13 auger parameters. If the shape of the auger is such that some of the parameters are not required, such as the FDP tip used in this model only needing height sections h_{s1} and h_{s2}, the unused parameters can be set to zero. Some of the soil parameters are also optional as approximate values can be calculated for them with the other parameters. These include ρ, δ and γ_s. By setting them to zero the models will calculate approximate values for them. In the future it is also possible to make files for all the available auger models, so the user does not have to input the values manually each time

they want to change the auger but instead can just run a different M-file with the corresponding values.

5 DISCUSSION

The goal of this thesis was to develop a Mevea based real-time simulation model of the Junttan MPx90 multipurpose rig to simulate CFA and FDP drilling in multilayered soils. Requirements for the model were real-time simulation speed, sufficient accuracy, and parametrization. The soil model should also be possible to implement in an existing pile driving simulation model. The main application for the model would be in R&D for control system development.

A literature review was done on the mechanics of CFA and FDP drilling to find out how the loading during these processes could be calculated. The results of the review revealed that drilling loading is generally assumed to be a result of soil friction, which generates torque and vertical force. The simulation models for both processes were based on the methods which seemed most promising. The CFA model was more complex, requiring several soil parameters. The FDP model was simpler and required only cone resistance of the soil.

As the drilling process cannot be modelled in Mevea, co-simulation had to be utilized. At the start of the project, it was decided that the co-simulation software would be either Xcos or Simulink. Based on performance comparisons done using a pile driving simulation model, Simulink was clearly superior, and the process models were made using it.

In order to validate the models, the simulated results were compared to measured torque and force values recorded during test drilling. Lack of detailed soil data in the testing site was a problem, but enough information was available to estimate the range of possible values. The FDP model produced good results for torque in particular. Simulated force was less accurate, but sufficient nonetheless. The measurements also showed a correlation between force and torque as the theory indicated. A notable weakness in the model is the inaccuracy in calculating force when the auger is not rotating. The CFA model on the other hand was more disappointing. The torque values were more accurate than the force values just like with the FDP model, but even they differ from the measured values. Borehole 4 displays very good correlation between simulated and measured torque though, so it is possible that the inaccuracy is caused by poor selection of soil values. There is a clear difference between

theory and the results from the test drilling. As vertical force and torque are generated by components of the same forces during the CFA process according to theory, there should be a noticeable correlation between them. This is reflected in the simulation results, as the force and torque curves have similar shapes. The measurements however show none of that. This indicates that there are other mechanisms at work during the process.

The models were deemed to produce sufficiently accurate results and meet their requirements. The developed Mevea model interfaced with the process models also fulfills the real-time speed requirement. The soil model can be exported to other models. In conclusion, the goals set for this thesis were met.

5.1 Future development

More development must be done on both models to improve simulation accuracy, but especially the accuracy of the force during a CFA process. The most preferable solution would be to conduct test drilling in an area where detailed measurement data from the soil is available, in order to minimize the number of assumptions that have to be made and ensure that any errors in the models are not caused by mistakes in soil parameters.

This thesis only covered two drilling methods and there many more which the MPx machines are used for. In the future, models for methods such as DTH (Down the Hole) and Kelly need to be developed.

As the model made in this thesis is only partial, a model of the entire MPx90 rig still needs to be developed in the future. This model can be used as a basis for it and expanded over time. Some of the rotary head’s functions are also missing since they were not required for the methods examined in this thesis.

LIST OF REFERENCES

Aksoy, H. S., Gör. M. & İnal, Esen. 2016. A New Design Chart for Estimating Friction Angle Between Soil and Pile Materials. In: Geomechanics and Engineering. Vol. 10: 3. Daejeon: Techno-Press. pp. 315–324.

BAUER Spezialtiefbau GmbH. 2018. BAUER Bored Piles [web document]. [Referred: 23.9.2020]. 16 p. Available in PDF-file: https://bauertech.co.uk/export/shared/documents/pdf/bst/print/905_015_2_BAUER-Bored-Piles_en.pdf.

Begemann, H. K. S. 1965. The Friction Jacket Cone as an Aid in Determining the Soil Profile. Proceedings of the 6th International Conference on Soil Mechanics and Foundation Engineering. Montreal, Quebec, Canada. 8-15.9.1965. pp. 17–20.

Carlsten, P. 1988. Torv – geotekniska egenskaper och byggmetoder. Linköping, Sweden: Swedish Geotechnical Institute. 34 p.

Chen, T., Zhao, Z., Wang, Q. & Wang, Q. 2018. Modeling and Experimental Investigation of Drilling into Lunar Soils. In: Applied Mathematics and Mechanics (English Edition). Vol. 40: 1. Springer Science and Business Media. 2019. pp. 153–166.

Damen Magazine. 2017. Accurate Accessibility Prediction for SOV Thanks to HIL Simulator. [Damen Magazine webpage]. Updated June 28, 2017. [Referred: 10.10.2020]. Available: https://magazine.damen.com/markets/offshore-wind/accurate-accessibility-prediction-for-sov-thanks-to-hil-simulator/

Douglas, B. J., & Olsen, R. S. 1981. Soil Classification Using Electric Cone Penetrometer. Proceedings of a Session Sponsored by the Geotechnical Engineering Division at the ASCE National Convention. St. Louis, Missouri. 26-30.10.1981. pp. 209–227.

Fellenius, B.H. & Eslami, A. 2000. Soil Profile Interpreted from CPTu Data. Year 2000 Geotechnics - Geotechnical Engineering Conference. Bangkok, Thailand. 27-30.11.2000. 18 p.

Fellenius, B.H. 2018. Basics of Foundation Design. Electronic Edition. Vero Beach: Pile Buck International. 466 p.

Godwin, R. J. & Spoor, G. 1977. Soil Failure with Narrow Tines. In: Journal of Agricultural Engineering Research. Vol. 22: 3. pp. 213–228.

Junttan Oy. 2020a. Junttan. [Junttan Oy webpage]. [Referred 3.9.2020]. Available: https://junttan.com/

Junttan Oy. 2020b. Multipurpose drilling rigs. [Junttan Oy webpage]. [Referred 3.9.2020]. Available: https://junttan.com/products/multipurpose-drilling-rigs/

Krasiński, A. 2014. Numerical Simulation of Screw Displacement Pile Interaction with Non-Cohesive Soil. In: Archives of Civil and Mechanical Engineering. Poland: Elsevier. Vol. 14: 1. pp. 122–133.

Krasiński, A. 2015. The Analysis of Soil Resistance During Screw Displacement Pile Installation. In: Studia Geotechnica et Mechanica. Vol.36: 3. Berlin: De Gruyter. pp. 49–56.

Liikennevirasto. 2012. Tien geotekninen suunnittelu. Liikenneviraston ohjeita 10/2012. Helsinki. 82 p.

Lunne, T., Powell, J.J.M. & Robertson, P.K. 1997 Cone Penetration Testing in Geotechnical Practice. London: Spon Press. 352 p.

MathWorks. 2020. Simulink – Simulation and Model-Based Design. [MathWorks webpage]. [Referred 18.11.2020]. Available: https://www.mathworks.com/products/simulink.html

Mevea Oy. 2020a. Mevea | Software and services to build your own digital twins. [Mevea Oy webpage]. [Referred 5.10.2020]. Available: https://mevea.com/

Mevea Oy. 2020b. Software for Real-Time Simulation. [Mevea Oy webpage]. [Referred 18.11.2020]. Available: https://mevea.com/solutions/software/

Mevea Oy. 2021. Simulators for sale and marketing. [Mevea Oy webpage]. Available: https://mevea.com/solutions/digital-twin/sales-marketing/

McKyes, E. & Ali, O. S. 1977. The cutting of soil by narrow blades. In: Journal of Terramechanics. Vol. 14: 2. Oxford: Pergamon Press. pp. 43–58.

Normet Oy. 2020. Normet Academy – Normet. [Normet Oy webpage]. [Referred 10.10.2020]. Available: https://www.normet.com/services/normet-academy/

Popovici, K. & Mosterman, P. J. 2017. Real-Time Simulation Technologies: Principles, Methodologies, and Applications. 1st Edition. Boca Raton: CRC Press. 660 p.

Prakesh, S. & Sharma, H. D. 1990. Pile Foundation in Engineering Practice. John Wiley & Sons. 768 p.

Pucker, T. & Grabe, J. 2012. Numerical Simulation of the Installation Process of Full Displacement Piles. In: Computers and Geotechnics. Vol. 45. Elsevier Ltd. pp. 93–106.

Reece, A.R. 1964. Paper 2: The Fundamental Equation of Earth-Moving Mechanics. In: Proceedings of the Institution of Mechanical Engineers, Conference Proceedings. Vol. 179: 6. pp. 16–22.

Robertson, P.K., Campanella, R.G., Gillespie, D. & Greig, J. 1986. Use of Piezometer Cone Data. Use of In-Situ Tests in Geotechnical Engineering: Proceedings of In-Situ ’86, a Specialty Conference. Geotechnical Special Publication No. 6. New York: American Society of Civil Engineers. pp. 1263–1280.

Robertson, P. K. 1990. Soil Classification Using the Cone Penetration Test. In: Canadian Geotechnical Journal. Vol. 27: 1. Ottawa: Canadian Science Publishing. pp. 151–158.

Robertson, P. K. & Cabal, K. L. 2012. Guide to Cone Penetration Testing for Geotechnical Engineering. 5th Edition. California: Gregg Drilling & Testing. 145 p.

Schmertmann, J. H. 1978. Guidelines for Cone Penetration Test: Performance and Design. Washington, D.C.: Department of Transportation, Federal Highway Administration. 145 p.

Scilab. 2020. About. [Referred: 18.11.2020]. Available: https://www.scilab.org/about

Shabana, A. A. 2005. Dynamics of Multibody Systems. 3rd Edition. Cambridge: Cambridge University Press. 386 p.

Shi, D., Yang, Y., Deng, Y. & Xue, J. 2019. DEM Modelling of Screw Pile Penetration in Loose Granular Assemblies Considering the Effect of Drilling Velocity Ratio. In: Granular Matter. Vol. 21: 74. Berlin: Springer. pp. 1–16.

Tian, Y., Tang, D., Deng, Z., Jiang, S. & Quan, Q. 2015. Drilling Power Consumption and Soil Conveying Volume Performances of Lunar Sampling Auger. In: Chinese Journal of Mechanical Engineering. Vol. 28: 3. Chinese Mechanical Engineering Society. 2015. pp. 451–459.

Verrujit, A. 2018. An Introduction to Soil Mechanics. Cham: Springer International Publishing. 420 p.

Zhang, T., Ding, X. 2016. Drilling Forces Model for Lunar Regolith Exploration and Experimental Validation. In: Acta Astronautica. Vol. 131. Elsevier Ltd. pp. 190–203.

Zhao, D., Tang, D., Hou, X., Jiang, S. & Deng, Z. 2016. Soil Chip Convey of Lunar Subsurface Auger Drill. In: Advances in Space Research. Vol. 57: 10. Elsevier Ltd. 2016. pp. 2196–2203.

CFA simulation results

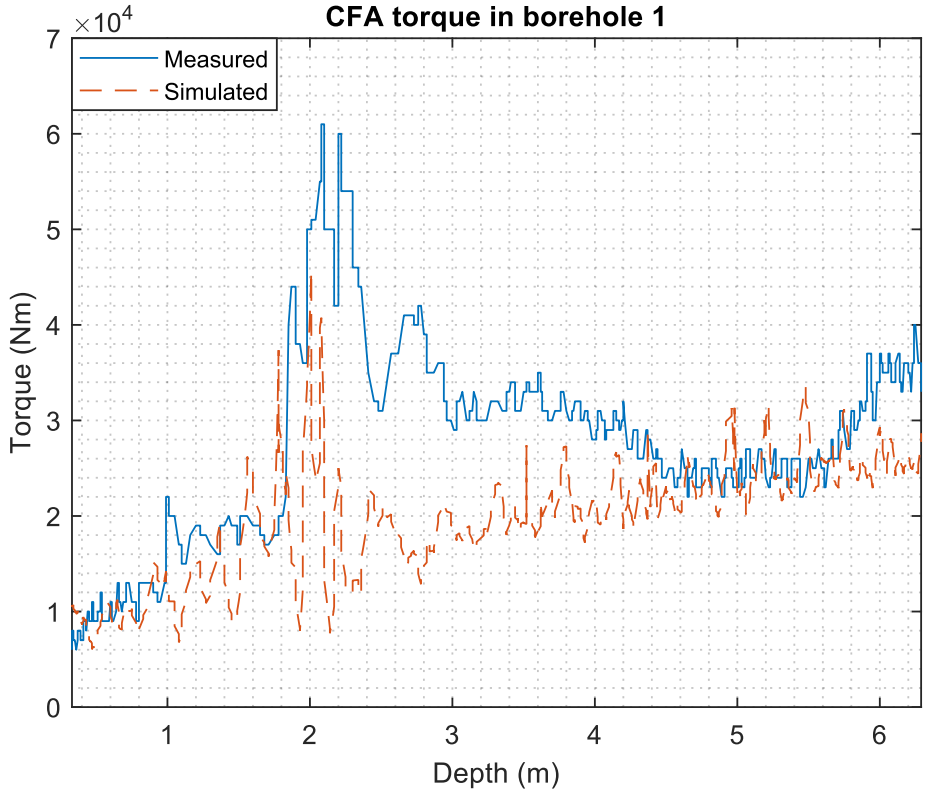

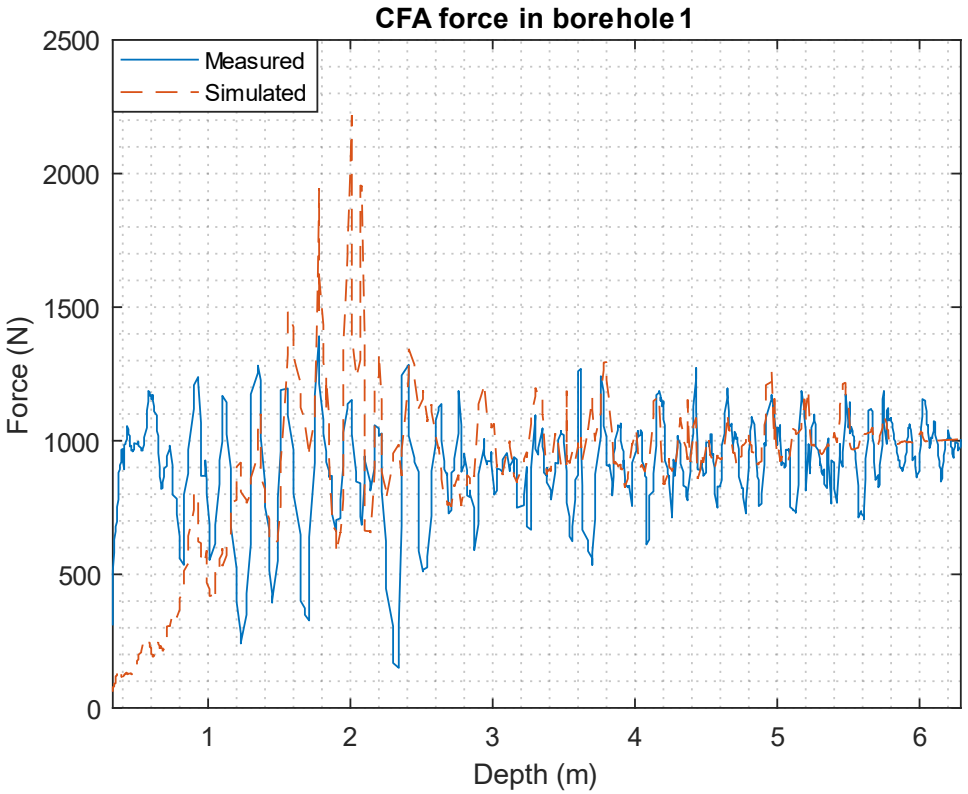

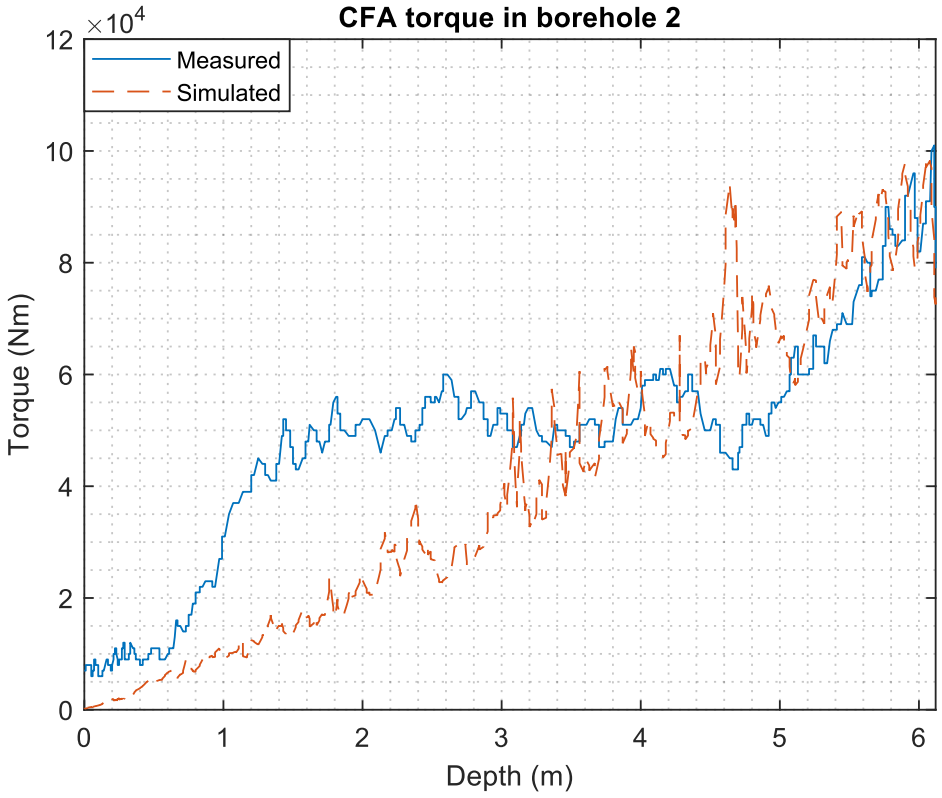
CFA torque in borehole 2
×10^4
Measured
Simulated
Torque (Nm)
Depth (m)
0
2
4
6
8
10
12
0
1
2
3
4
5
6

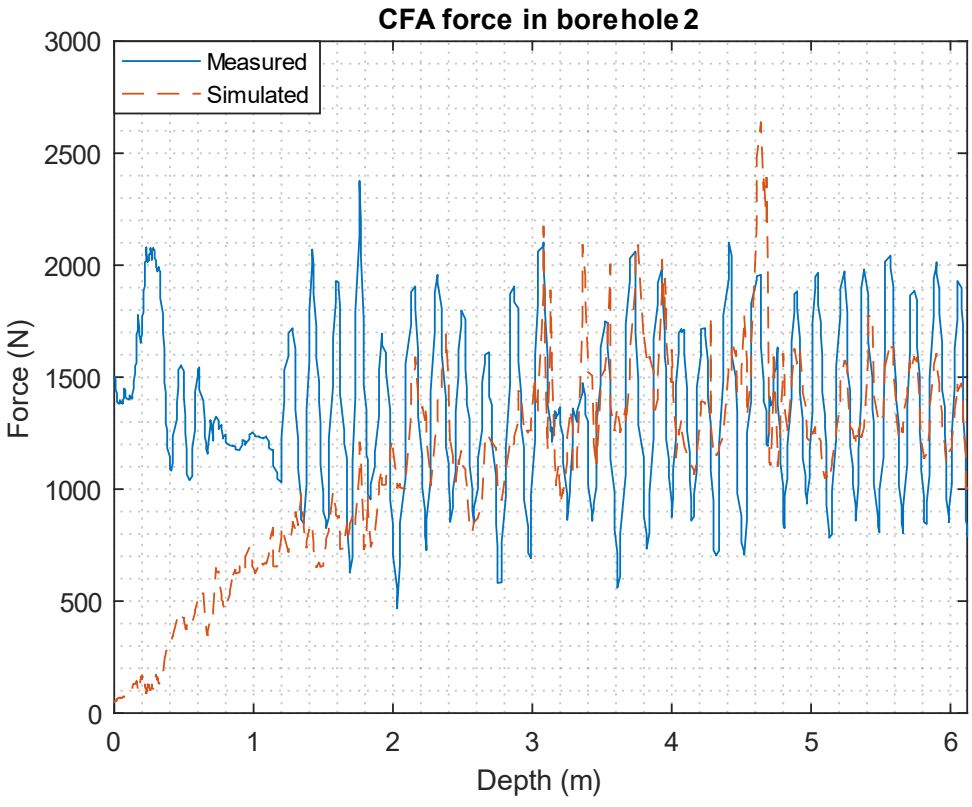
CFA force in borehole 2
Measured
Simulated
Force (N)
Depth (m)
0
500
1000
1500
2000
2500
3000
0
1
2
3
4
5
6

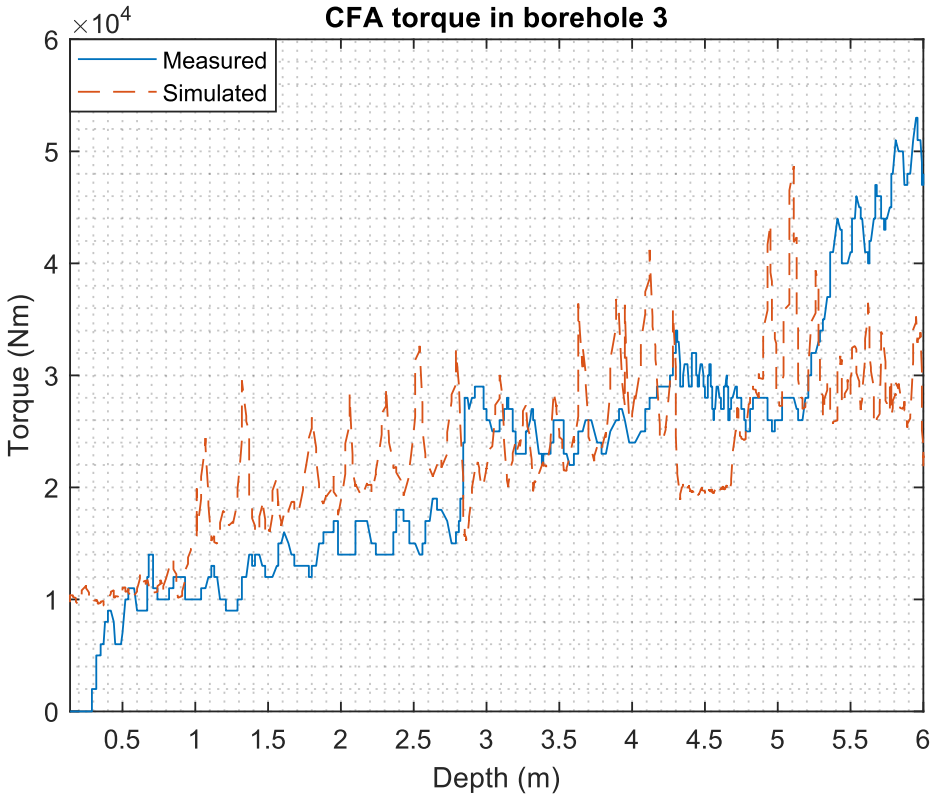
CFA torque in borehole 3
×10^4
Measured
Simulated
Torque (Nm)
Depth (m)
0
1
2
3
4
5
6
0.5
1
1.5
2
2.5
3
3.5
4
4.5
5
5.5
6

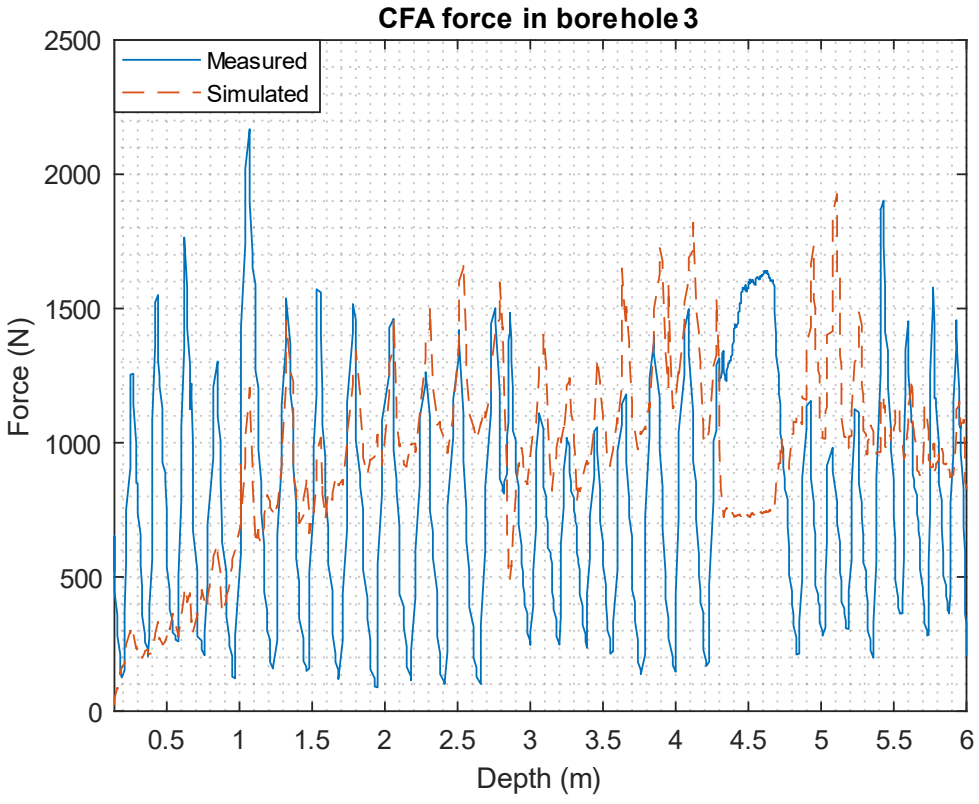
CFA force in borehole 3
Measured
Simulated
Force (N)
Depth (m)
0
500
1000
1500
2000
2500
0.5
1
1.5
2
2.5
3
3.5
4
4.5
5
5.5
6

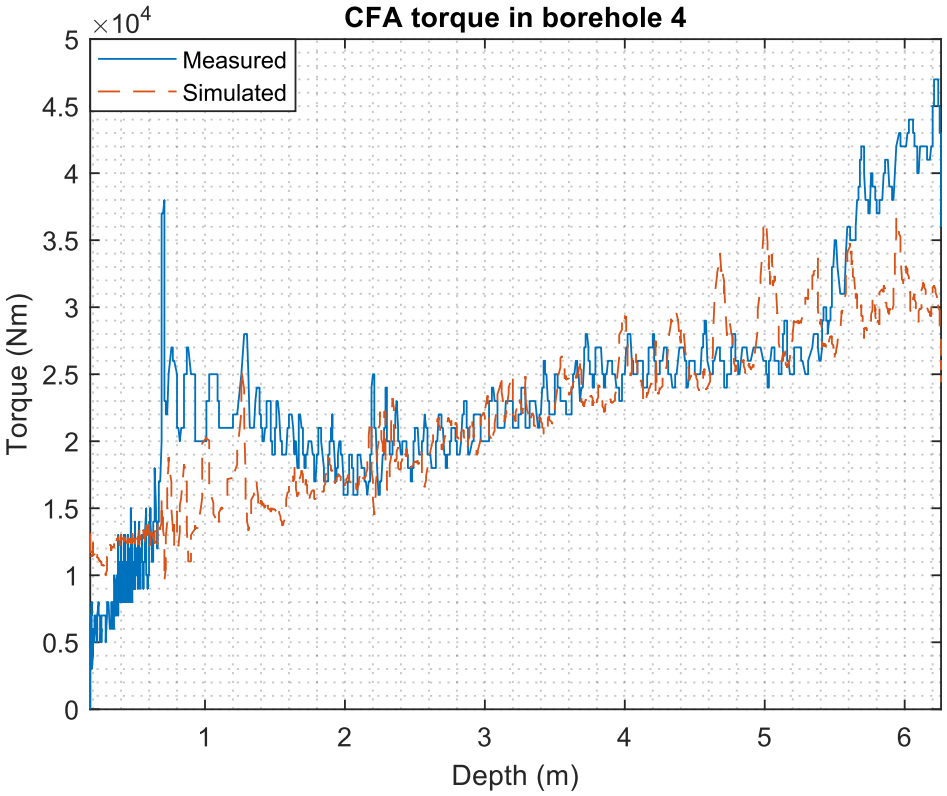
CFA torque in borehole 4
×10^4
Measured
Simulated
Torque (Nm)
Depth (m)
0
0.5
1
1.5
2
2.5
3
3.5
4
4.5
5
1
2
3
4
5
6

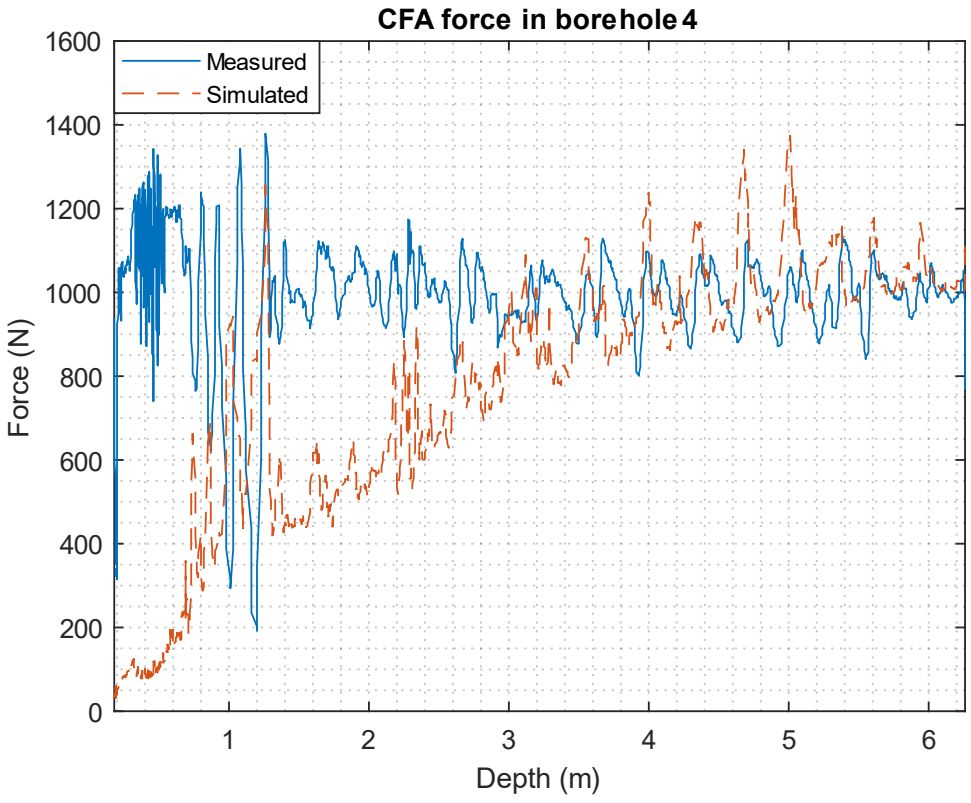
CFA force in borehole 4
Measured
Simulated
Force (N)
Depth (m)
0
200
400
600
800
1000
1200
1400
1600
1
2
3
4
5
6

FDP simulation results

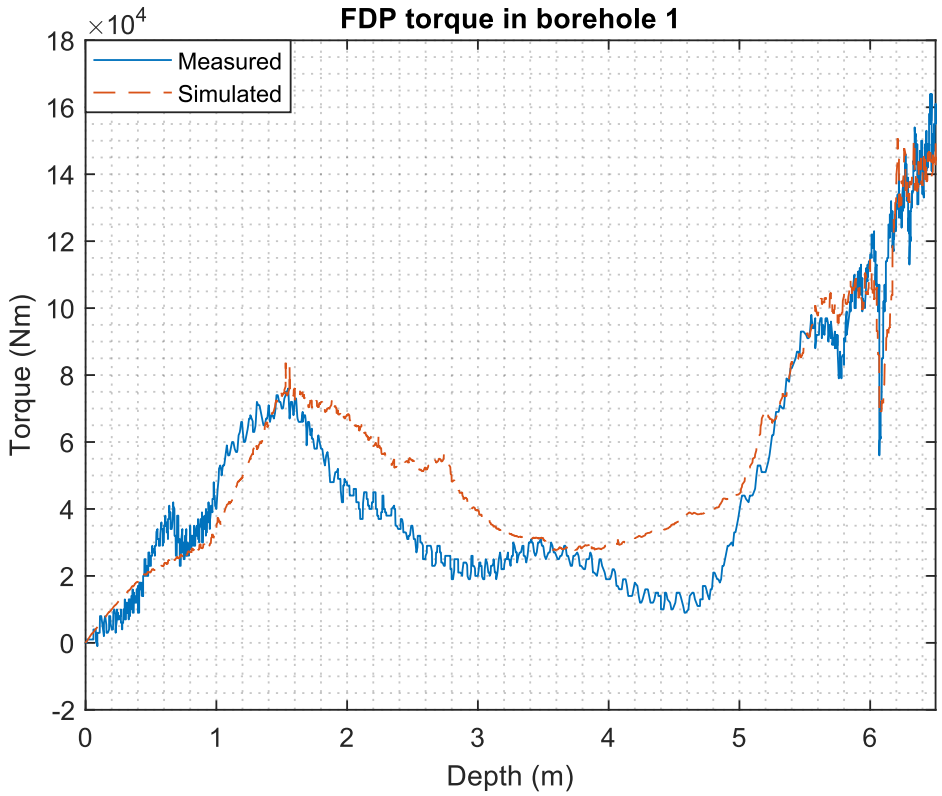

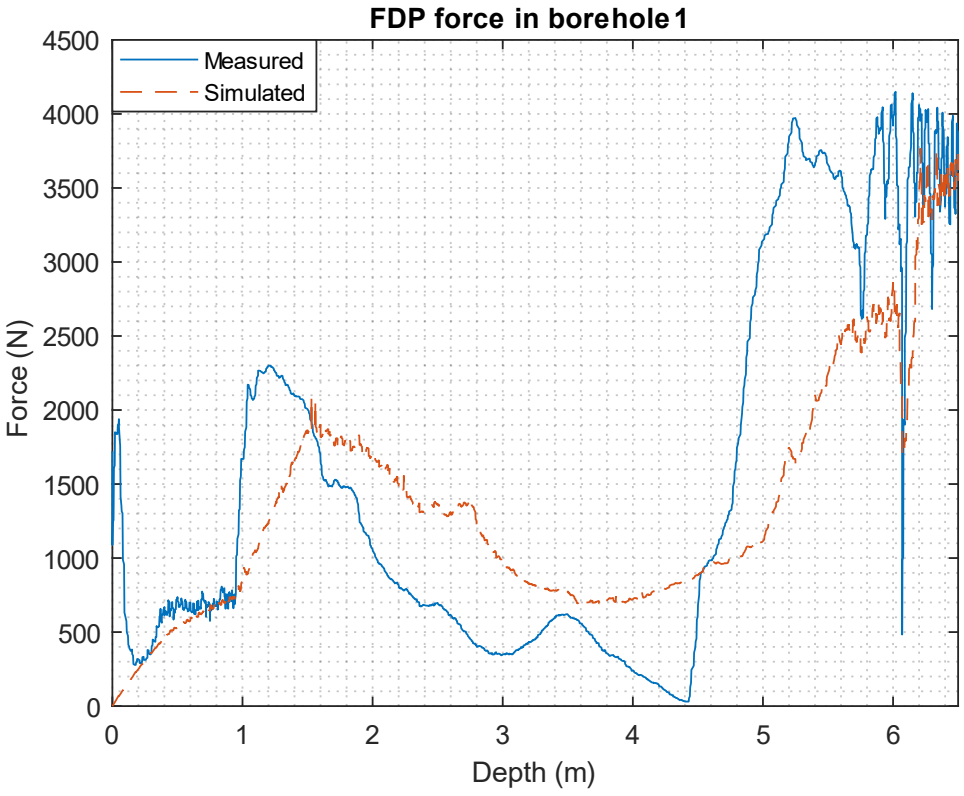

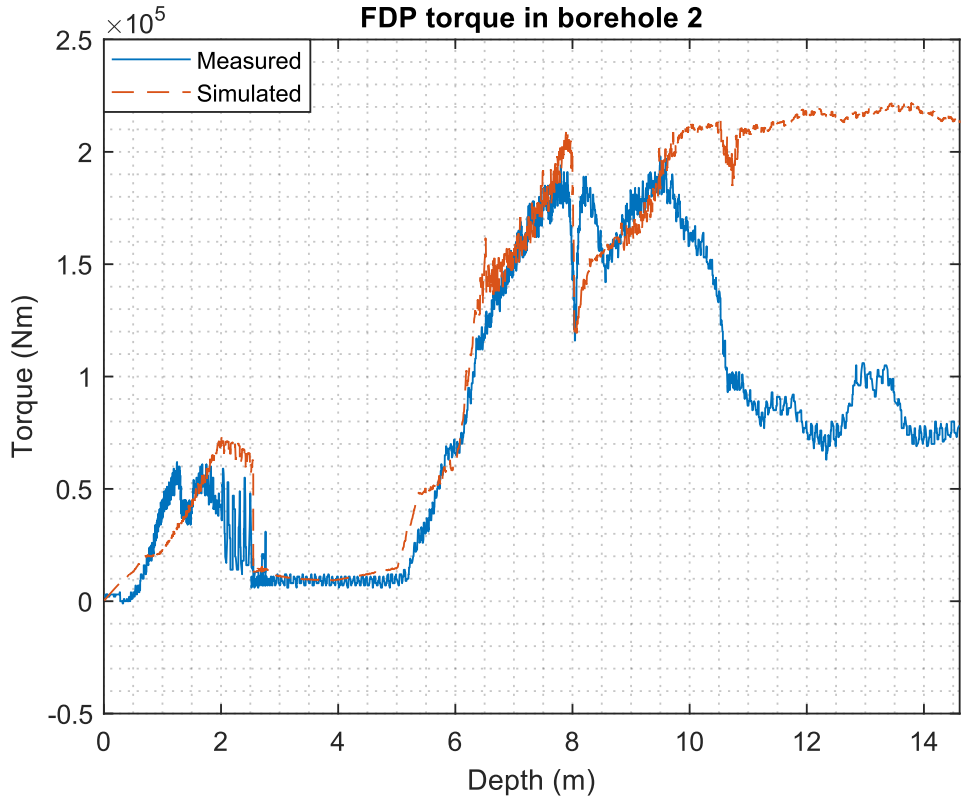
FDP torque in borehole 2
×10^5
Measured
Simulated
Torque (Nm)
Depth (m)
2.5
2
1.5
1
0.5
0
-0.5
0
2
4
6
8
10
12
14

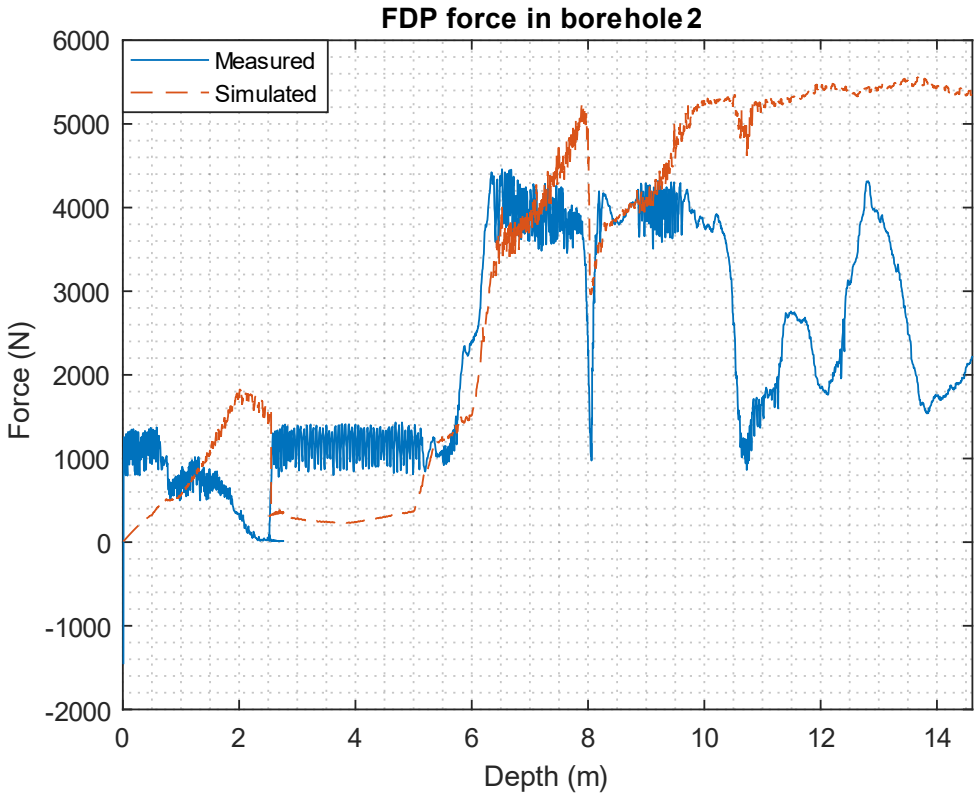
FDP force in borehole 2
Measured
Simulated
Force (N)
Depth (m)
6000
5000
4000
3000
2000
1000
0
-1000
-2000
0
2
4
6
8
10
12
14

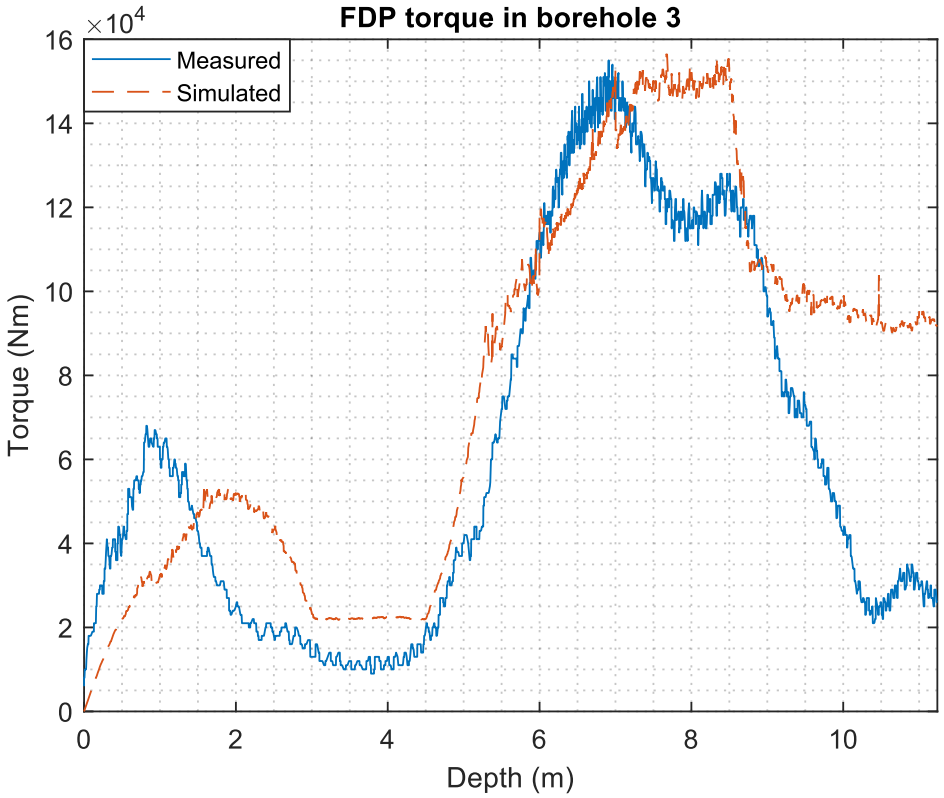
FDP torque in borehole 3
×10^4
Measured
Simulated
Torque (Nm)
Depth (m)
0
2
4
6
8
10
12
14
16

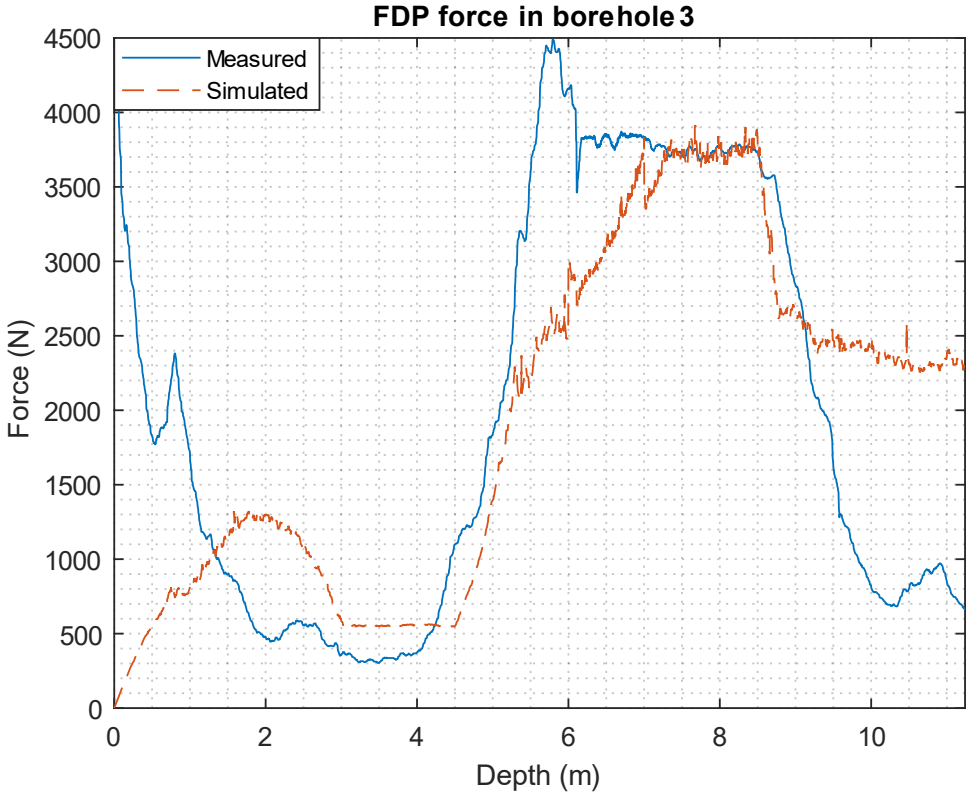
FDP force in borehole 3
Measured
Simulated
Force (N)
Depth (m)
0
500
1000
1500
2000
2500
3000
3500
4000
4500

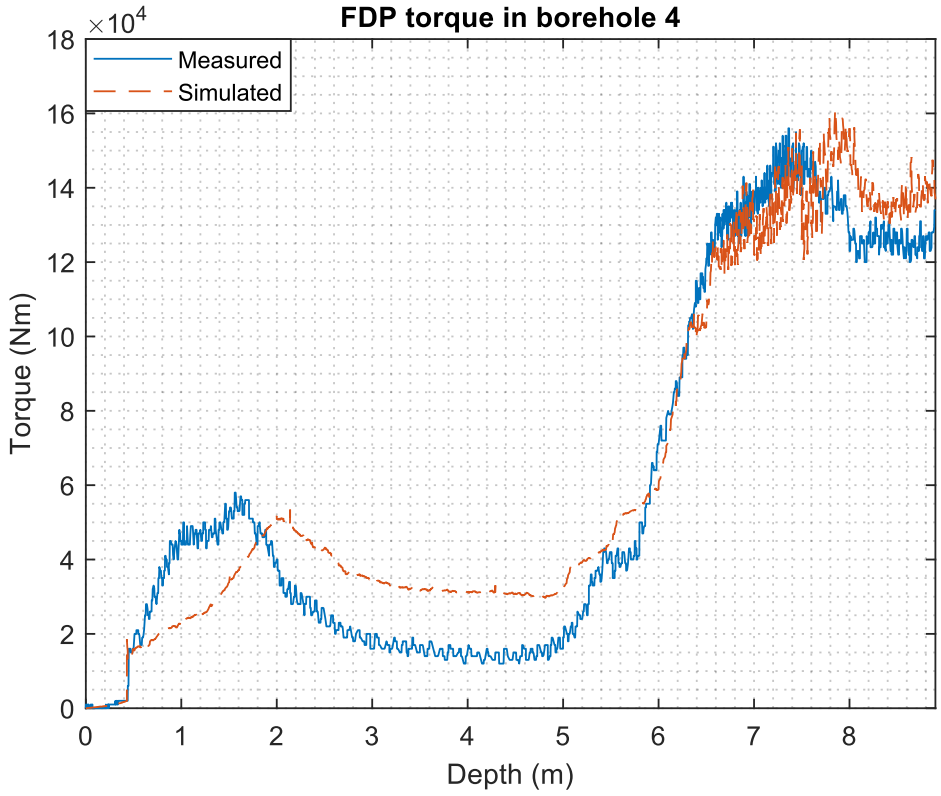
FDP torque in borehole 4
×10^4
Measured
Simulated
Torque (Nm)
Depth (m)
0
2
4
6
8
10
12
14
16
18
0
1
2
3
4
5
6
7
8

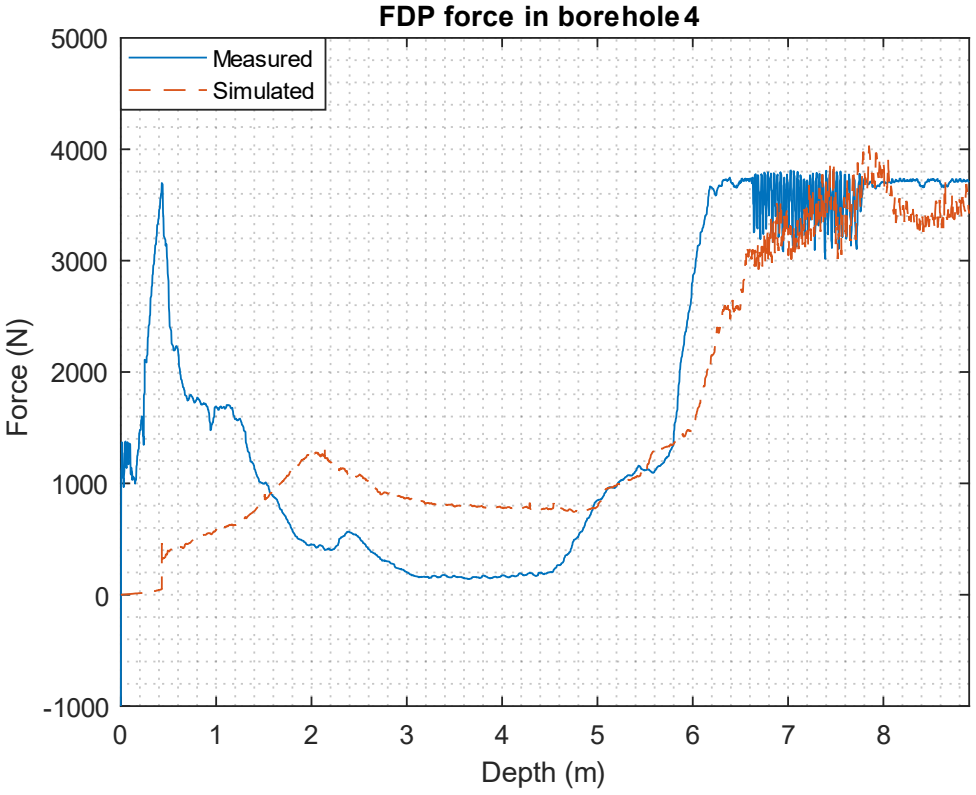
FDP force in borehole 4
Measured
Simulated
Force (N)
Depth (m)
-1000
0
1000
2000
3000
4000
5000
0
1
2
3
4
5
6
7
8

APPENDIX III

Mevea model